Structural and Energetic Properties of Weak Noncovalent Interactions in Two Closely Related 3,6-Disubstituted-[1,2,4]triazolo[3,4-b][1,3,4]thiadiazole Derivatives: In Vitro Cyclooxygenase Activity, Crystallography, and Computational Investigations

Lamya H. Al-Wahaibi, Sekar Karthikeyan, Olivier Blacque, Amal A. El-Masry, Hanan M. Hassan, M. Judith Percino, Ali A. El-Emam,* and Subbiah Thamotharan*

ACCESS | Metrics & More | Article Recommendations | Supporting Information

ABSTRACT: Two 3,6-disubstituted-[1,2,4]triazolo[3,4-b][1,3,4]thiadiazole derivatives, namely, 3-(adamantan-1-yl)-6-(2-chloro-6-fluorophenyl)-[1,2,4]triazolo[3,4-b][1,3,4]-thiadiazole **1** and 6-(2-chloro-6-fluorophenyl)-3-phenyl-[1,2,4]triazolo[3,4-b][1,3,4]-thiadiazole **2**, were prepared, and the detailed analysis of the weak intermolecular interactions responsible for the supramolecular self-assembly was performed using X-ray diffraction and theoretical tools. Analyses of Hirshfeld surface and 2D fingerprint plot demonstrated the effect of adamant-1-yl/phenyl moieties on intermolecular interactions in solid-state structures. The effect of these substituents on H···H/Cl/N contacts was more specific. The CLP-PIXEL and density functional theory methods provide information on the energetics of molecular dimers observed in these compounds. The crystal structure of compound **1** stabilizes with a variety of weak intermolecular interactions, including C−H···N, C−H···π, and C−H···Cl hydrogen bonds, a directional C−S···π chalcogen bond, and unconventional short F···C/N contacts. The crystal structure of compound **2** is stabilized by π-stacking interactions, C−H···N, C−H···π, and C−H···Cl hydrogen bonds, and highly directional attractive σ−hole interactions such as the C−Cl···N halogen bond and the C−S···N chalcogen bond. In addition, S(lp)···C(π) and short N···N contacts play a supportive role in the stabilization of certain molecular dimers. The final supramolecular architectures resulting from the combination of different intermolecular interactions are observed in both the crystal packing. The molecular electrostatic potential map reveals complementary electrostatic potentials of the interacting atoms. The quantum theory of atoms in molecules approach was used to delineate the nature and strength of different intermolecular interactions present in different dimers of compounds **1** and **2**. The in vitro experiments suggest that both compounds showed selectivity against COX-2 targets rather than COX-1. Molecular docking analysis showed the binding pose of the compounds at the active sites of COX-1/2 enzymes.
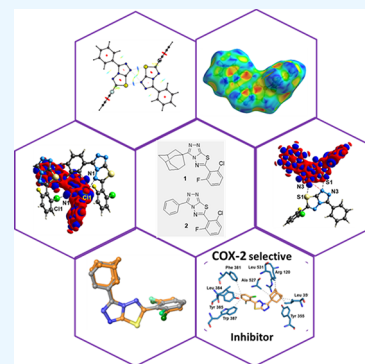
1. INTRODUCTION

In recent years, 1,2,4-triazoles and their fused heterocyclic derivatives received considerable attention owing to their diverse biological activities.[1,2] Several 1,2,4-triazoles were reported to possess potent anti-inflammatory,[3−9] antifungal,[10,11] antibacterial,[12,13] and anticancer activities.[14−16] On the other hand, the 1,3,4-thiadiazole heterocycle was early recognized as the core pharmacophore of numerous bioactive agents,[17−20] possessing marked anti-inflammatory[21−23] and anticancer activities.[24,25] Moreover, the hybrid triazole-thiadiazole derivative, 1,2,4-triazolo[3,4-b][1,3,4]thiadiazole, was recently reported to possess marked anticancer[26−29] and antibacterial activities[30,31] in addition to anti-inflammatory activity via selective inhibition of the cyclooxygenase COX-2 isoform.[32−34]

In continuation of our ongoing studies on the inhibitory selectivity of COX-1/2 of 1,2,4-triazoles[35] and 1,2,4-triazolo-[3,4-b][1,3,4]thiadiazoles,[36] we report herein the synthesis, structural analysis, and COX-1/2 inhibitory activity of two 1,2,4-triazolo[3,4-b][1,3,4]thiadiazole derivatives. Khan et al. synthesized libraries of triazolothiadiazole and triazolothiadiazine derivatives, which displayed remarkable cholinesterase and monoamine oxidase inhibitory properties.[37] In their study, the crystal structure of one of the triazolothiadiazole derivatives, 3-

(3-bromophenyl)-6-(*o*-tolyloxymethyl)-[1,2,4]triazolo[3,4-*b*]-[1,3,4]thiadiazole, was reported as the first 1,2,4-triazolo[3,4-*b*][1,3,4]thiadiazole structure that exhibits a short chalcogen bond [C=S⋯N: 2.795 (2) Å and 163.9 (2)°]. At that time, a Cambridge Structural Database (CSD) search revealed that no structure with a triazolothiadiazole ring system contained a short contact between the S atoms and N donors in the crystal structure, which was significantly shorter than 3.0 Å. In addition to this chalcogen bond, the π-stacking interaction formed between the planar aryl-substituted triazolothiadiazole moieties and the C−H⋯π interaction also involved in the stabilization of the crystal structure. In another study,[38] the authors evaluated the S⋯N chalcogen bond and the short N⋯N contact found in the same centrosymmetric dimer using a 3D-deformation density map, an electrostatic potential map, and quantum theory of atoms in molecules (QTAIM) parameters.

In the present investigation, we describe the molecular conformation and the role of noncovalent interactions in the crystal packing of two closely related 1,2,4-triazolo[3,4-*b*][1,3,4]thiadiazole derivatives, namely, 3-(adamantan-1-yl)-6-(2-chloro-6-fluorophenyl)-[1,2,4]triazolo[3,4-*b*][1,3,4]-thiadiazole **1** and 6-(2-chloro-6-fluorophenyl)-3-phenyl-[1,2,4]triazolo[3,4-*b*][1,3,4]thiadiazole **2**, in which adamantane and phenyl substituents are introduced in the core skeleton. The effect of adamantane and phenyl substituents has been characterized employing different computational tools, including the Hirshfeld surface (HS), molecular electrostatic potential (MESP) map, Bader's QTAIM, and noncovalent interaction plot (NCIPlot). The PIXEL energy calculation helps identify energetically potential dimers within crystal structures. The crystal structure of **1** is primarily stabilized by intermolecular C−H⋯N, C−H⋯Cl, and C−H⋯ π hydrogen bonds and a highly directional σ−hole (chalcogen bond) C−S⋯C(π) interaction in addition to unconventional F⋯C/N contacts. Similarly, the crystal structure of **2** is stabilized by intermolecular C−H⋯N, C−H⋯Cl, C−H⋯π, and C−H⋯F hydrogen bonds, weak π⋯π stacking interactions, and directional σ−hole interactions, including a C−S⋯N chalcogen bond and a Cl⋯N halogen bond. In addition, an unconventional lp⋯ π contact is also observed in one of the dimers of **2**. These noncovalent interactions play a critical role in the synthesis and stabilization of supramolecular architectures of numerous organic and inorganic compounds relevant to medicine, materials science, and catalysis.[39]

It is known that two cyclooxygenase (COX-1 and COX-2) enzymes have been involved in the inflammatory cell signaling pathway in an arachidonic acid-dependent manner. Selective inhibition of COX-2 can reduce the adverse reactions, including ulcerogenic effects of non-steroidal anti-inflammatory drugs such as acetylsalicylic acid and ibuprofen.[40] In the present investigation, we demonstrated the effect of the adamantane moiety on the anti-inflammation potential using two closely related derivatives of triazolothiadiazole. Further, we described the observed bioactivity of the title compounds using an in vitro COX-1/2 assay, molecular docking, and molecular mechanics with generalized Born and surface area solvation (MM-GBSA) analyses.

2. RESULTS AND DISCUSSION

The purpose of this study is to investigate the effect of the adamantane and phenyl groups introduced in the core skeleton of the triazolothiadiazole ring on crystal packing and

intermolecular interactions using various computational approaches. With the support of the in vitro data from the COX-1/2 assay, in silico molecular docking and free energy calculation, we describe the effect of the adamantane group on the observed biological activity.

2.1. Chemical Synthesis. The investigated compounds **1** and **2** were prepared using the following reaction sequences outlined in Scheme 1. The corresponding carboxylic acid

Scheme 1. Synthetic Pathway for the Title Compounds 1 and 2
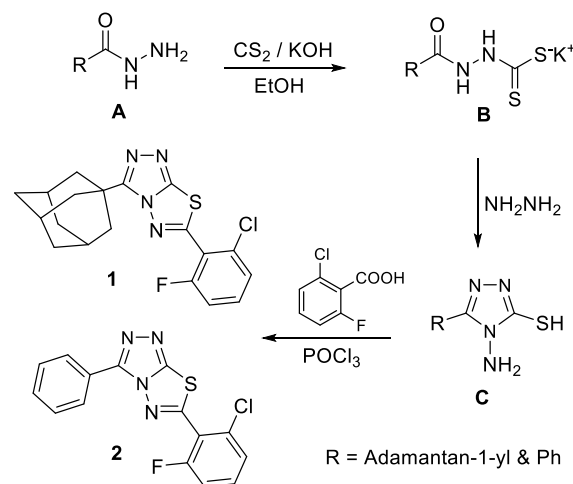
hydrazide **A** was treated with carbon disulfide in an ethanolic potassium hydroxide solution to yield the corresponding potassium dithiocarbazate intermediates **B**, which were subsequently reacted with hydrazine to produce the corresponding 4-amino-5-substituted-4*H*-1,2,4-triazole-3-thiols **C**.[41,42] Compounds **C** were then reacted with 2-chloro-6-fluorobenzoic acid and phosphorous oxychloride by heating under reflux for 2 hours to produce target compounds **1** and **2** in yields of 84 and 72%, respectively.

2.2. Description of Molecular and Crystal Structures. For the two closely related triazolothiadiazoles, a low-temperature (160 K) single-crystal structure determination has been performed to delineate the effect of adamantan-1-yl (compound **1**) and phenyl (compound **2**) moieties attached at position 3 (C9) carbon of the triazolothiadiazole ring on molecular conformation, crystal packing, and intermolecular interactions. Both compounds have a 2-chloro-6-fluorophenyl substituent at position 6 (C7) to study their role in crystal packing and intermolecular interactions. The X-ray analysis revealed that both compounds crystallize in the monoclinic system, and one molecule is present in the respective asymmetric unit. In compound **1**, the 2-chloro-6-fluorophenyl ring was disordered over two orientations with the site occupation factors of 0.7764(19) for the major disordered component. This major disordered component was used for all analyses reported in this work. Crystallographic data and refinement parameters for compounds **1** and **2** are presented in Table 1, and their thermal ellipsoid representations are shown in Figure 1.

The central triazolothiadiazole unit makes a right angle (86.6°) with the mean plane of the adamantane cage in compound **1**, whereas the unsubstituted phenyl ring is nearly coplanar (3.4°) with the central triazolothiadiazole moiety in compound **2**. We note that the orientation of the 2-chloro-6-

Table 1. Crystal Data and Structure Refinement Parameters for Compounds 1 and 2

	compound 1	compound 2
empirical formula	$C_{19}H_{18}ClFN_4S$	$C_{15}H_8ClFN_4S$
formula weight	388.88	330.76
crystal system	monoclinic	monoclinic
space group	$P2_1/n$	$P2_1/c$
a/Å	13.0790(2)	11.1796(3)
b/Å	11.69139(17)	15.4566(5)
c/Å	13.3373(2)	8.3228(2)
α/°	90	90
β/°	117.769(2)	93.499(2)
γ/°	90	90
volume/Å^3	1804.55(6)	1435.49(7)
Z	4	4
ρ_{calc} g/cm^3	1.431	1.530
μ/mm^{-1}	3.130	3.832
F(000)	808.0	672.0
crystal size/mm^3	0.25 × 0.21 × 0.14	0.32 × 0.2 × 0.02
radiation	Cu Kα (λ = 1.54184)	
2Θ range for data collection/°	7.82 to 148.9	7.924 to 148.986
index ranges	$-11 \leq h \leq 16$, $-14 \leq k \leq 14$, $-16 \leq l \leq 13$	$-13 \leq h \leq 12$, $-15 \leq k \leq 19$, $-9 \leq l \leq 10$
reflections collected	18687	11943
crystal size/mm^3	0.25 × 0.21 × 0.14	0.32 × 0.2 × 0.02
independent reflections	3685 [R_{int} = 0.0176, R_{sigma} = 0.0088]	2923 [R_{int} = 0.0336, R_{sigma} = 0.0284]
data/restraints/parameters	3685/501/297	2923/0/199
goodness-of-fit on F^2	1.061	1.073
final R indexes [$I \geq 2\sigma$ (I)]	R_1 = 0.0436, wR_2 = 0.1144	R_1 = 0.0432, wR_2 = 0.1145
final R indexes [all data]	R_1 = 0.0441, wR_2 = 0.1149	R_1 = 0.0598, wR_2 = 0.1252
largest diff. peak/hole/e Å^{-3}	0.69/−0.33	0.69/−0.72
CCDC no.	2122999	2123000

fluorophenyl ring is nearly perpendicular to the mean plane of the central unit in both structures (75.4° in **1** and 83.0° in **2**). The Mogul geometry check suggests that both structures do not show unusual bond lengths or angles. However, it should be mentioned that the C7−S1 bond [1.761(1) Å in compound **1** and 1.757(1) Å in **2**] exhibits bond lengthening compared to the C8−S1 bond [1.738(1) Å in **1** and 1.728(1) Å in **2**]. A similar feature has been observed in related structures deposited in the CSD (version 5.42, November 2020).[43] This bond lengthening could be due to the formation of a σ−hole interaction (chalcogen bond). Furthermore, the CSD search detected 51 hits containing different substituents attached to atom C9 of the triazole ring and atom C7 of the thiadiazole ring. Five of these compounds have an adamantane cage attached to a thiadiazole ring (CSD refcodes: BOTYEP, UPAVIR, VUNLUM, VUNMAT, and WADHIU).[44−47] Unlike compound **1**, which has an adamantane cage attached to a triazole ring, we identified eight structures containing monosubstituted (CSD refcodes: NITSIV, ILETOK, LEPQED, QEMMUR, and SAPRAD, UXIPOI),[36,48−52] disubstituted (CSD refcode: XOYWOZ),[53] and trisubstituted (csd refocde: GAJCUS)[38] halophenyl groups. The halogen atoms are either Cl or F or both present at different positions of the phenyl ring. Contrary to compounds **1** and **2**, the substituted phenyl ring in these structures is coplanar with the central triazolothiadiazole ring. This planarity could be

maintained due to the formation of intramolecular S⋯X (X = Cl or F) contact in all structures mentioned above except in 6-(4-chlorophenyl)-3-(thiophen-2-yl)-[1,2,4]triazolo[3,4-b]-[1,3,4]-thiadiazole (UXIPOI).[52] In this structure, Cl was substituted in the para position of the phenyl ring and does not participate in the S⋯Cl contact.

For a deeper understanding of why title compounds **1** and **2** do not exhibit either S⋯Cl or S⋯F intramolecular contact (or why disubstituted phenyl adopts non-coplanar with central unit?), as well as to uncover the energy barriers associated with it, we performed a relaxed potential surface scan around the C7−C1 bond in compound **2** at the B3LYP/6-31G+(d) level of theory (Figure 2). The result suggests that the conformer "*a*" is the least energy conformer for the S1−C7−C1−C6 torsion angle of ±90°, which is very similar to that of the X-ray conformer (−97.08°). In the second least energy conformer "*b*", S and F atoms are displaced on the same side, whereas in the high energy conformer "*c*", S and Cl atoms are oriented on the same side. The energy difference between the conformers "*a*" and "*b*" is 2.8 kcal mol^{-1}, while the corresponding energy difference for the conformers "*b*" and "*c*" is only 1.3 kcal mol^{-1} (4.0 kcal mol^{-1} for the conformers "*a*" and "*c*"). This analysis demonstrates that the twisted orientation of the disubstituted phenyl ring has minimum energy on its potential energy surface, and a molecular conformation with S⋯F/Cl contact has a higher energy range from 2.8 to 4.0 kcal mol^{-1} concerning the minimum energy conformer.

As shown in Figure S1, the molecular conformation of compound **1** is stabilized by two intramolecular C−H⋯N interactions. Similarly, compound **2** has an intramolecular C−H⋯N interaction. The topological analysis confirms the existence of these interactions (Table S1). Some of the related structures are also stabilized by an intramolecular C−H⋯N interaction as observed in compounds **1** and **2** (CSD refcodes for these structures are given in Supporting Information: see Table S2).[36−38,44,48,49,52−63] Due to the existence of this intramolecular interaction, the central triazolothiadiazole moiety becomes coplanar with the substituent group attached to the triazole ring at atom C9 (corresponding atom in the related structures). In other structures, the substituent group on the triazole ring is slightly twisted to the mean plane of the central unit due to the lack of an intramolecular C−H⋯N interaction.

2.3. Hirshfeld Surface Analysis and 2D Fingerprint Plots. Hirshfeld surface (HS) analysis has been widely used to qualitatively determine the intermolecular contacts within crystal structures. HS and decomposed 2D fingerprint (FP) plots reveal the effect of the phenyl and adamantane moieties on the intermolecular interactions. Figure 3a shows the HS over the d_{norm} values for compounds **1** and **2**. In compound **1**, the intense red spots are shown for the intermolecular C−H⋯N hydrogen bond and an attractive σ−hole interaction such as a chalcogen bond of type S⋯C(π) and an unorthodox bifurcated fluorine bond of type F⋯C/N contacts.

In compound **2**, the S⋯N chalcogen bond shows intense and broad red surfaces, and a short N⋯N contact also shows an intense spot near the chalcogen interacting region (Figure 3b). This feature suggests that the chalcogen bond along with a short N⋯N contact plays a significant role in the stabilization of the crystal structure. The relatively less intense spots were observed for C−H⋯N, C−H⋯Cl, and Cl⋯N interactions. Over the five-membered ring, we observed less intense red spots due to the π-stacking interaction. We also observed tiny
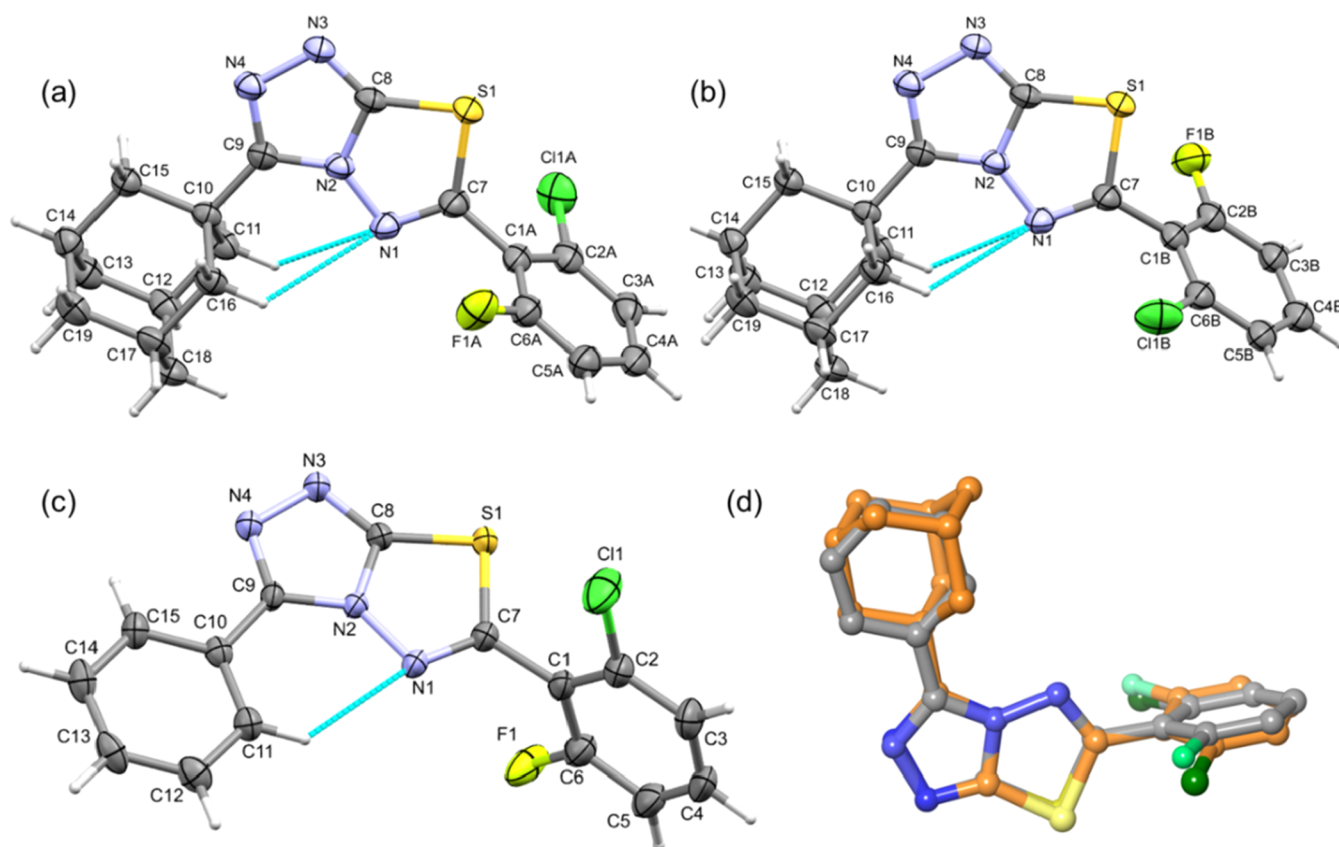
Figure 1. Thermal ellipsoid plots of compounds (a) **1** (major disordered component), (b) **1** (minor disordered component), and (c) **2** drawn at the 50% probability level. (d) Structural superimposition of structures **1** (major disordered component: orange) and **2** (gray).
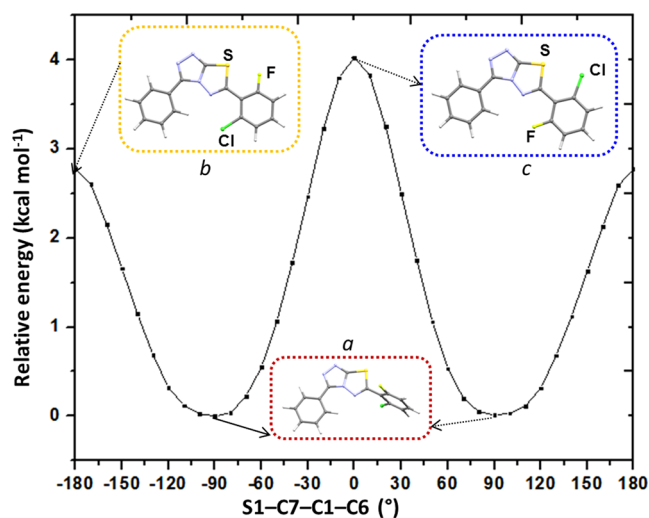

Figure 2. Calculated potential energy for rotation around the C7−C1 bond in structure **2**.

red spots for the S(lp)···C(π) contact in the same π-stacking dimer, which might provide additional stabilization to this dimer.

The 2D-FP plots show distinct distribution patterns for intercontacts in **1** and **2** (Figures 4, S2 and S3, Supporting Information). The intermolecular H···H interactions occupy most of the HS area toward the crystal packing of these structures. Due to the adamantane cage in compound **1**, the H···H contacts increase (38.6%) and those in compound **2** decrease (19.7%) due to the phenyl ring. The next significant

contribution comes from H···N contacts (14.3% in **1** and 13.1% in **2**), and the contribution of these contacts is comparable. Furthermore, this contact shows double spikes on the 2D-FP and the tip distance is at 2.3 Å in compound **1**, whereas the corresponding contact beyond 2.5 Å in compound **2** indicates a relatively weak nature. The contributions of other inter-contacts such as H···C (11% in **1** and 13.9% in **2**) and H···S (6.3% in **1** and 7.2% in **2**) interactions are comparable. We note that the shortest $d_i + d_e$ distance for H···C contacts is very similar in these structures and located around 2.8 Å. The inter-H···S contacts are located beyond 3.0 Å, which is longer than the sum of the vdW radii, and these contacts may not have a significant role in stabilizing crystal structures. It is observed that the H···Cl contacts influence the crystal packing, and the relative contribution of this contact is higher in compound **1** (12.5%) than in compound **2** (7.2%). The shortest $d_i + d_e$ distance is located for this contact at 2.8 Å in compound **2** and 3.0 Å in compound **1**, suggesting that the short H···Cl contact plays a significant role in the stabilization of the crystal structure of compound **2**.

In contrast to the H···Cl contact, the contribution of H···F contact is higher in compound **2** (9.2%) than in compound **1** (3.3%). The shortest $d_i + d_e$ distance appears more extended than the sum of the vdW radii of H and F atoms suggesting that the H···F contact plays a minor role in stabilization. Additionally, the inter-C···C contacts, which represent π-stacking interactions, contribute about 4.9% to compound **2**, and the corresponding contact contributes only 0.3%, indicating its absence in the crystal structure of compound **1**. The shape index plot shows the presence or absence of π-stacking in compounds **2** and **1**, respectively (Figure 4).
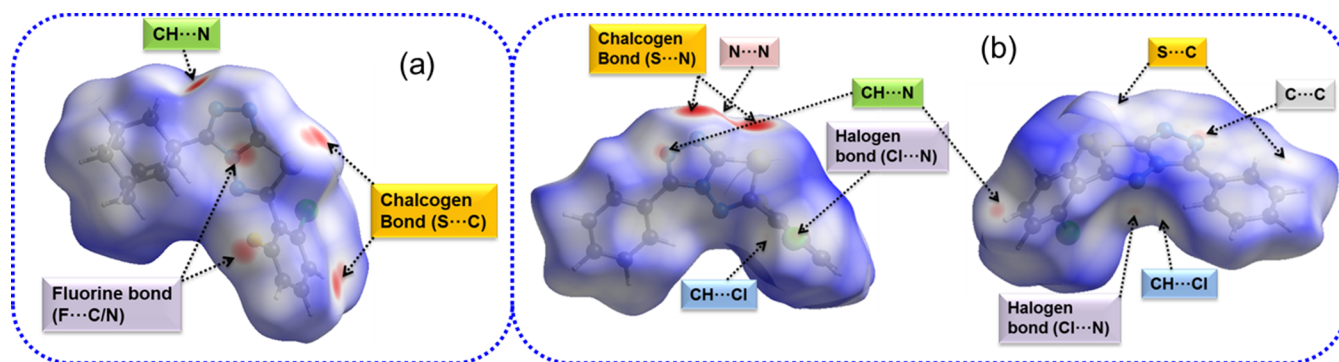
Figure 3. HSs show red spots corresponding to the close intercontacts observed in structures (a) **1** and (b) **2** in two different orientations.
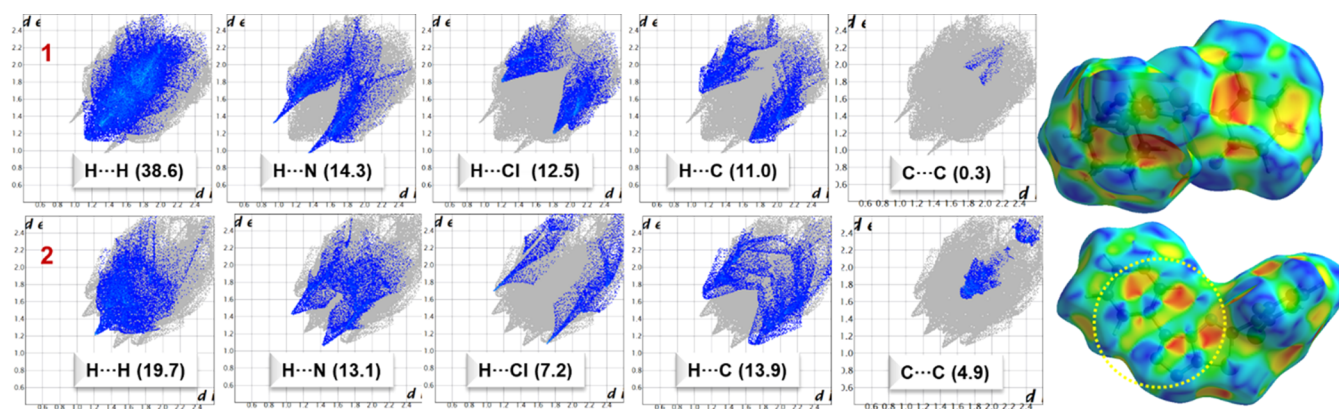

Figure 4. 2D-fingerprint plots for selected intercontacts were observed in crystal structures of compounds **1** and **2**. The shape index diagram (on the last column) shows red and blue triangles (dot circled) over the phenyl and triazole rings, indicating the presence of π-stacking interaction in compound **2**.

In addition to the intermolecular interaction mentioned above, the contribution of some inter-contacts is relatively less compared to other contacts. For instance, F···C and F···N contacts contribute each about 1.9% and a highly directional S···C(π) chalcogen bond contributes only 2.0% to the crystal packing of compound **1** yet plays a significant role in stabilizing the crystal structure.

2.4. Crystal Packing. *2.4.1. Crystal Packing of Compound 1.* In the solid state, the molecules of compound **1** are packed in a columnar way along the crystallographic *ac* plane (Figure 5a). CLP-PIXEL energy analysis revealed six dimers (D1–D6; Figure 5a–e) in the crystal structure of compound **1**, and the intermolecular interaction energies for these dimers range from −12.7 to −3.8 kcal mol^{-1}. These energies for most dimers are comparable to those calculated by the density functional theory (DFT) method with the B97D3/def2-TZVP level of approximation. As shown in Figure 5a, the primary structural motif (dimer D3) is stabilized by an intermolecular C−H···C(π) interaction between the adamantyl moiety and the phenyl ring. This interaction links the neighboring molecules into a C(10) chain that runs parallel to the crystallographic *b* axis (Figure S4). Furthermore, the D3 dimer is stabilized with an 80% dispersion energy component. The most stable dimer D1 stabilizes with the three centered F1A··· C8/N2 contacts. The stabilization of dimer D1 is further supported by an intermolecular C−H···N interaction, which makes a R$_2^2$(18) motif. Furthermore, the dispersion and electrostatic energy components contribute 59 and 41%, respectively, toward the stabilization of dimer D1. As shown

in Figure 5a, the primary structural motifs in the adjacent columns are interconnected by dimeric motif D1.

The second most stable dimer D2 is formed by two intermolecular C−H···π interactions involving H atoms of the adamantane and triazolothiadiazole core, with a dispersion energy contribution of approximately 74% for stabilization. These C−H···π interactions interconnect the neighboring molecules into a chain which runs parallel to the crystallographic *a* axis (Figure S5). Dimer D4 is formed by a highly directional chalcogen bond of type C−S···C(π) interaction, which links the adjacent molecules into a C(6) chain that runs parallel to the crystallographic *b* axis (Figure S6). The electrostatic (51%) and dispersion (49%) energy components are nearly equal to the stabilization of this dimer.

Dimer D5 is stabilized by an intermolecular C−H···N interaction, and this interaction links neighboring molecules into a C(10) chain that runs parallel to the crystallographic *b* axis. Moreover, the electrostatic energy contributes about 65% toward the stabilization of this dimer. The least stable cyclic dimer [D6; R$_2^2$(22) motif] is formed by intermolecular C−H··· Cl interactions. The H···Cl contact distance is slightly longer (by 0.06 Å) than the sum of the vdW radii of H and Cl atoms and Cl atoms. For stabilization, the dispersion energy contributes about 79%.

In addition, different intermolecular interactions observed in **1** are combined to form a supramolecular self-association in the solid state. The basic structural motif D3 and the dimeric motif D5 combined to assemble a molecular ribbon that runs parallel to the *b* axis. Further, three molecules of **1** generate a loop utilizing two D3 and a D5 motifs (Figure 6a). As shown
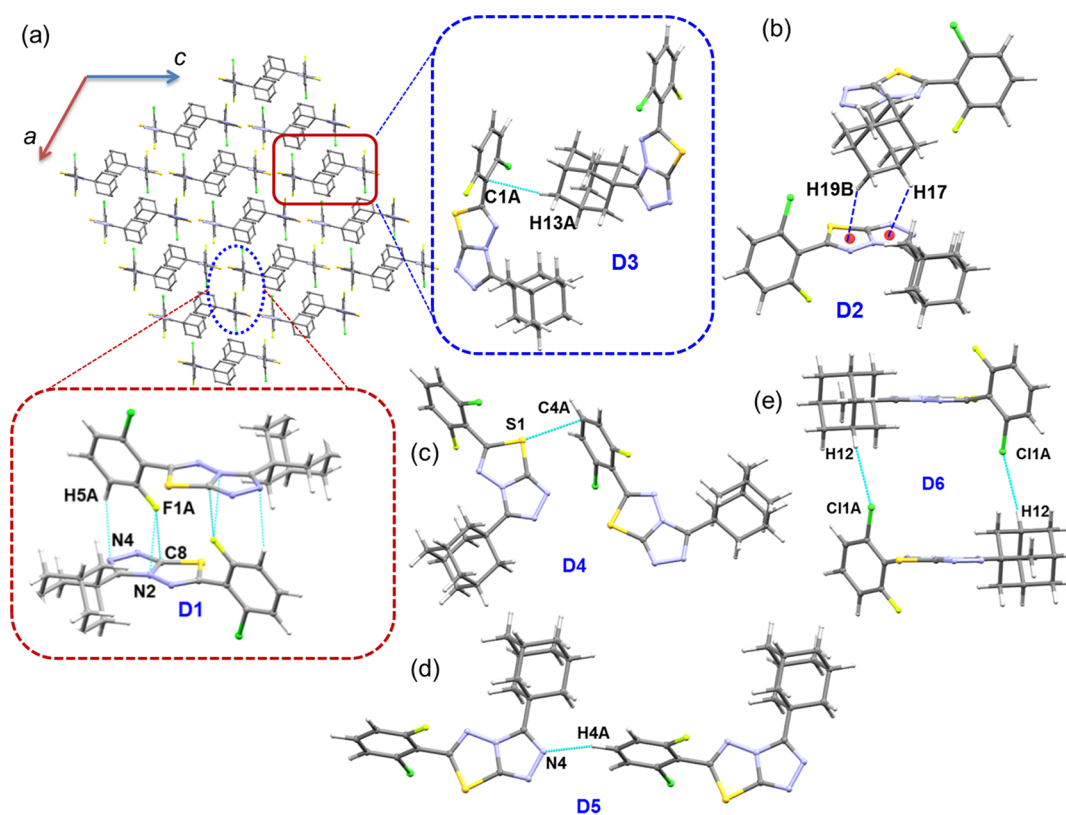
Figure 5. (a) Columnar arrangement of the molecule of compound **1** in the solid state; basic structural motifs are boxed (dimers D1 and D3). (b−e) Other molecular dimers (D2, D4, D5, and D6) formed in the crystal structure of **1** by different non-covalent interactions.
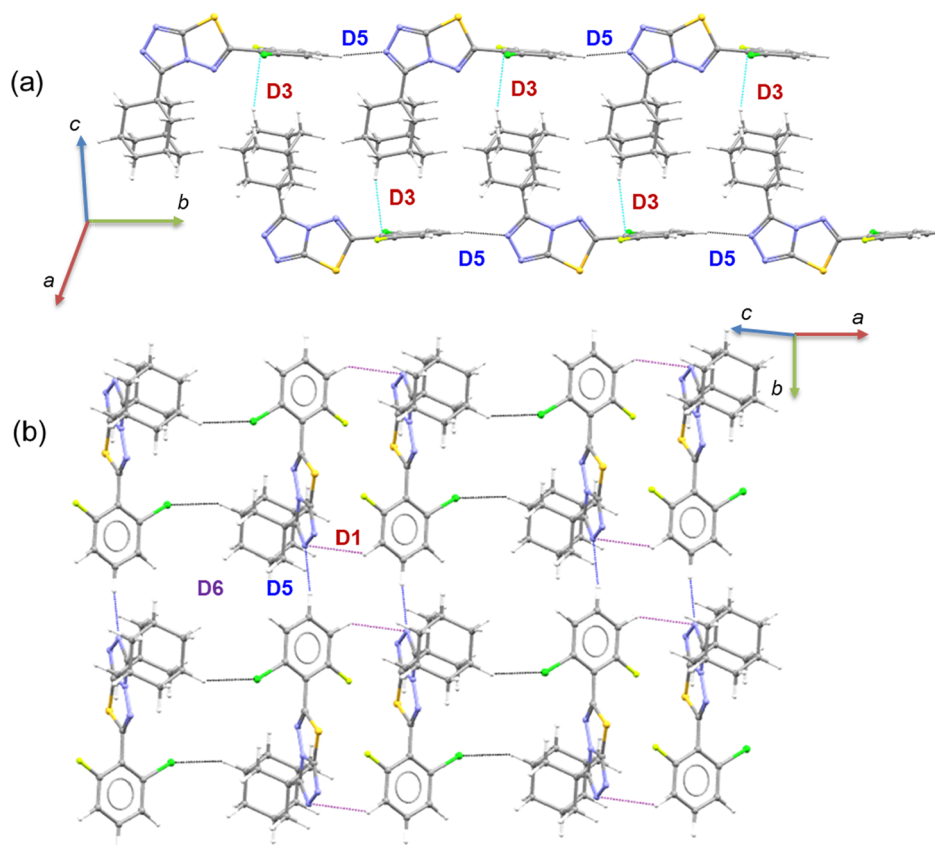

Figure 6. Supramolecular self-assembly built by (a) motifs D3 and D5 and (b) motifs D1, D5, and D6.

in Figure 6b, two intermolecular C−H···N interactions (dimers D1 and D5) and a weak C−H···Cl (dimer D6) interaction collectively generate a supramolecular sheet. The adjacent loops formed by this weak C−H···Cl interaction interlinked by C−H···N interactions in both the directions. As mentioned above, the chalcogen bonding (dimer D4) interaction alone generates a molecular chain and forms a molecular ribbon when the chalcogen bond is combined to C−H···N interactions (dimer D5) and this molecular ribbon runs parallel to the *b* axis (Figure S7).

Furthermore, we calculated the MESP map for compound **1** to understand the molecule's charge distribution and gain further insights into the observed intermolecular interactions in the solid states (Figure 7). On the MESP map, we can see that
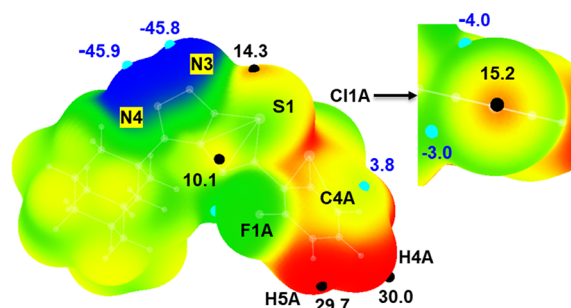

Figure 7. MESPs for the structure of compound **1** and the electron density surface drawn at 0.001 au contour. Color scales (in kcal mol^{-1}): red: >15; yellow: 15 to 0, green: 0 to −25; and blue: >−25. The small hemispheres indicate the positive ($V_{s,max}$; black) and negative ($V_{s,min}$; blue) electrostatic potentials for selected atoms along with their values. The close-up view shows σ−holes for the Cl atom and a characteristic negative belt.

the protons of the di-substituted phenyl ring had the most positive electrostatic potentials ($V_{s,max}$) compared to the H atoms of the adamantane moiety. The most negative electrostatic potentials ($V_{s,min}$) are observed for atoms N4 (−45.9 kcal mol^{-1}) and N3 (−45.8 kcal mol^{-1}) of the triazole ring. Atoms H4A ($V_{s,max}$: 30.0 kcal mol^{-1}) and H5A ($V_{s,max}$: 29.7 kcal mol^{-1}) have participated as donors for the intermolecular C−H···N interactions with triazole N4 atoms having the most negative electrostatic potential. The lone pair of F1A atom with a $V_{s,min}$ value of −10.4 kcal mol^{-1} is likely to make F···π contact (dimer D1) with the π-hole over the surface of C8−N2 bond with a $V_{s,max}$ value of 10.1 kcal mol^{-1}. The MESP map also reveals the σ−hole for the S atom with the positive electrostatic potential at the tip of the C7− S1 bond with a $V_{s,max}$ value of 14.3 kcal mol^{-1} and this atom forms a directional chalcogen bond (C−S···π type) with atom C4A(π). On the MESP map, we observed a negative electrostatic potential with a $V_{s,min}$ value of 3.8 kcal mol^{-1} near the C4A atom. From the calculated MESP map, we can also see the σ−hole for the Cl atom with a $V_{s,max}$ value of 15.2 kcal mol^{-1} at the tip of the C−Cl bond and the negative belt around Cl atom corresponds to lone pairs. It is interesting to note that there is no σ−hole interaction involving the Cl atom. However, the lone pair of the Cl atom makes a weak C−H···Cl hydrogen bond (dimer D6) with the H atom of the adamantane moiety.

2.4.2. Crystal Packing of Compound 2. In the solid state, the molecules of compound **2** are also columnar packed in the crystallographic *bc* plane, but somewhat different from the crystal packing of molecule **1** (Figure 8). CLP-PIXEL energy

analysis identifies four dimers (D1−D4) with significant intermolecular interaction energies (E_{tot}) observed in this structure (Table 2). These energies range from −11.1 to −6.3 kcal mol^{-1}. The energy values are comparable to those calculated by the DFT method with the B97D3/def2-TZVP level of theory. The basic structural motif (dimer D1) consists of inversion-related molecules stabilized by π-stacking interactions between phenyl and triazole rings (Figure 8a). The π-stacked dimer D1 is further strengthened by weak lp···π (involving atoms S1 and C14) and C−H···F interactions. The latter hydrogen bond is established slightly longer than the sum of the vdW radii of the H and F atoms and makes an $R_2^2(20)$ ring motif.

The second strong dimer (D2) is also formed between inversion-related molecules and stabilized by C7−S1···N3 chalcogen bonds and further reinforced by a short N···N (triazole···triazole) contact with a distance of 2.89 Å (Figure 8b). It is important to note that the electrostatic energy contributes 77% toward stabilizing dimer D2. The NCI (non-covalent interaction index) analysis was performed to visualize the nature of the interactions formed in this dimer based on electron density ($ρ$) and its reduced density gradient (s). The NCI plot shows a strong attractive nature of a chalcogen bond compared to the N···N contact formed in the same dimer. A similar feature has been observed in the related structure reported in the literature.[38]

Dimer D3 stabilizes with intermolecular C−H···π inter-actions and three centered interactions. The Cl atom acts as an acceptor for C−H···Cl interactions and as a donor for a halogen bond of type C−Cl···N interactions. For stabilization of this dimer, the dispersion energy contributes about 76% (Figure 8c). The least stable dimer (D4) in this structure is stabilized by the three-centered C−H···N interaction ($R_2^1(5)$ring motif) in which one of the triazole nitrogens (atom N4) acts as an acceptor (Figure 8d). This interaction links the molecules into a chain that runs parallel to the crystallographic *a* axis. The electrostatic energy contributes about 61% toward the stabilization of this dimer. It is observed that the adjacent dimers of D1 are interlinked by D3 dimer runs that alternately form a molecular ribbon (Figure 8e). We also observed that adjacent dimers of D2 are interconnected by dimer D3 that forms a herringbone-like supramolecular architecture (Figure 8f).

Furthermore, the deformation density map was calculated for dimers D2 and D3 to visualize σ−hole interactions (chalcogen and halogen bonds). Figure 9a shows the deformation density map displaying the charge concentration region (blue) near the N3 atom and charge depletion region (red) closer to the S1 atom. These features suggest the existence of the S···N chalcogen bond in dimer D2 (Figure 9a). Similarly, the charge concentration region is located near the N1 atom and the charge depletion region around the Cl1 atom, suggesting the presence of a highly directional Cl···N halogen bond (Figure 9b).

To further understand the formed interactions in compound **2**, MESP map was computed. The MESP map of compound **2** shows that the most positive electrostatic potentials ($V_{s,max}$) are observed for protons of the di-substituted phenyl ring, which are higher than H atoms of the phenyl ring. This feature is very similar to that of compound **1**. The H atoms of the di-substituted phenyl ring act as donors for intermolecular C−H···N interactions with atom N4 ($V_{s,min}$: −41.7 kcal mol^{-1}). The most positive electrostatic potential surface near atoms H4
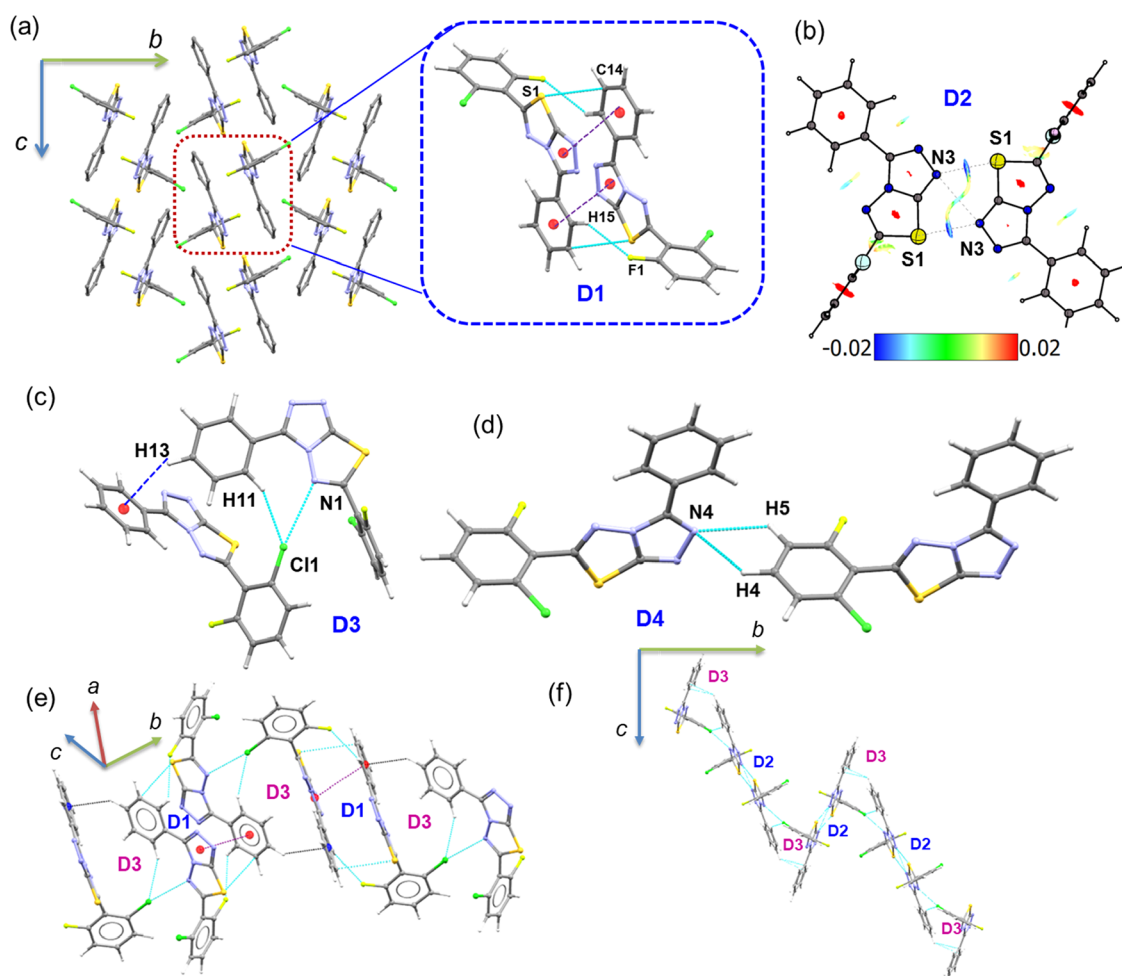
Figure 8. (a) Crystal packing of compound **2** and its basic structural motif (D1) is highlighted. (b−d) Molecular pairs (D2−D4) of compound **2** held together by different types of non-covalent interactions. (e) Formation of a supramolecular ribbon by alternate dimers of D3 and D1. (f) Herringbone-like supramolecular architecture built by alternate dimers of D3 and D2.

($V_{s,max}$: 31.3 kcal mol^{-1}) and H5 ($V_{s,max}$: 31.0 kcal mol^{-1}). Complementary electrostatic potentials facilitate the formation of C−H⋯N interactions. The MESP map also reveals the σ−hole at the tip of the C−Cl bond with a $V_{s,max}$ value of 15.8 kcal mol^{-1} and a characteristic negative belt around the Cl atom ($V_{s,min}$: −4.0 to −0.2 kcal mol^{-1}). The Cl makes an attractive σ−hole halogen bond (C−Cl⋯N) with the lone pair of N1 atom having a negative electrostatic potential value of −9.4 kcal mol^{-1}. As observed in **1**, the S1 atom shows σ−hole (17.6 kcal mol^{-1}) and makes an attractive chalcogen bond (C−S⋯N) with atom N3 having the negative electrostatic potential value of −43.0 kcal mol^{-1}. Atom H11 with a positive ESP value of 10.2 kcal mol^{-1} is likely to participate in a weak intermolecular C−H⋯Cl hydrogen bond with the negative belt of the Cl atom.

2.5. Topological Analysis of Intermolecular Interactions in Compounds 1 and 2.
The intermolecular interactions observed in various dimers of compounds **1** and **2** were characterized using the topological properties. The topological properties for the selected interactions in these dimers are summarized in Table 3. The molecular graphs showing the intermolecular interactions at the bond critical points in different dimers of compounds **1** and **2** are illustrated in Figures S8 and S9. The positive values of Laplacian of the electron density ($\nabla^2\rho(r) > 0$) and total electronic energy

density ($H(r) > 0$) and $|−V(r)/G(r)| < 1$ indicate all the observed intermolecular interactions in compounds **1** and **2** are closed-shell in nature. In compound **1**, the dissociation energy values (D_e) suggest that the C−H⋯N (dimer D4) interaction is found to be more assertive with a value of 2.9 kcal mol^{-1}, compared to other interactions. The next strongest interaction is the F⋯N contact with a D_e value of 1.9 kcal mol^{-1}. The chalcogen bond of type S⋯π showed a similar strength with that of F⋯N contact. The other two interactions, C−H⋯N (dimer D1) and C−H⋯Cl (dimer D6) showed similar strength.

In compound **2**, the chalcogen bond (S⋯N, D_e = 4.2 kcal mol^{-1}) and N⋯N contact (D_e = 2.7 kcal mol^{-1}) in dimer D1 showed significant strength compared to other interactions. The topological parameters for these contacts are comparable with the same contacts observed in the triazolothiadiazole derivatives reported earlier.[38] We also note that the strength of Cl⋯N halogen bond (dimer D3) is comparable with the strength of one of the C−H⋯N interactions observed in dimer D4. As expected, the intermolecular C−H⋯Cl bond is slightly weaker than C−H⋯N interactions.

2.6. In Vitro COX Inhibition Assay and Molecular Docking Analysis.
The synthesized compounds in this study were subjected to evaluate the anti-inflammation potentials against two important enzymes (COX-1 and COX-2) involved

Table 2. Intermolecular Interaction Energies (in kcal mol⁻¹) for Different Dimers Observed in the Crystal Structures of Compounds 1 and 2

dimer	CD	symmetry	important interactions	geometry H···A (Å), ∠ D−H···A (°)^a	E_{Coul}	E_{pol}	E_{disp}	E_{rep}	E_{tot}	ΔE_{cp}/B97D3/def2-tzvp
							PIXEL/MP2/6-31G**			
			compound **1** (major disordered component)							
D1	5.897	−x + 1, −y + 1, −z + 1	C5−H5A···N4	2.74, 137	−6.4	−1.7	−11.6	7.0	−12.7	−12.8
			F1A···C8	2.920 (1)						
			F1A···N2	2.939 (1)						
D2	8.124	x − 1/2, −y + 3/2, z − 1/2	C19−H19B···Cg1	2.63, 151	−2.6	−1.5	−11.5	7.7	−7.9	−8.4
			C17−H17···Cg2	2.84, 125						
D3	8.708	−x + 1/2, y − 1/2, −z + 3/2	C13A−H13A···C1A(π)	2.89, 145	−1.6	−0.9	−10.0	6.0	−6.5	−8.0
D4	9.185	−x + 1/2, y − 1/2, −z + 1/2	C7−S1···C4A(π)	3.186 (1), 170.5 (1)	−4.3	−2.9	−6.9	8.4	−5.7	−6.7
D5	11.691	x, y − 1, z	C4A−H4A···N4	2.27, 161	−5.9	−2.3	−4.4	7.0	−5.7	−5.2
D6	7.605	−x, −y + 1, −z + 1	C12−H12···Cl1A	3.01, 133	−0.9	−0.3	−4.4	1.8	−3.8	−4.1
			compound **2**							
D1	6.491	−x + 1, −y + 1, −z + 1	Cg1···Cg2	3.509 (1)	−4.8	−3.3	−19.1	16.1	−11.1	−13.5
			S1(lp)···C14(π)	3.475 (1)						
			C15−H15···F1	2.67, 125						
D2	8.039	−x + 1, −y + 1, −z + 2	C7−S1···N3	2.803 (1), 164.8 (1)	−18.5	−9.1	−8.1	26.4	−9.3	−10.4
			N3···N3	2.886 (1)						
D3	5.834	x, −y + 1/2, z + 1/2	C11−H11···Cl1	2.79, 152	−2.4	−1.7	−13.2	9.1	−8.4	−9.4
			C2−Cl1···N1	3.223 (1), 170.0 (1)						
			C13−H13···Cg2	2.85, 145						
D4	11.180	x − 1, y, z	C4−H4···N4	2.50, 128	−4.4	−1.6	−3.9	3.6	−6.3	−5.4
			C5−H5···N4	2.74, 117						

^{a}Neutron values are given for all D−H···A interactions. CD: distance between geometrical centers of molecules. In compound **1**: Cg1: S1−C7−N1−N2−C8; Cg2: N2−C8−N3−N4−C9. In compound **2**: Cg1: N2−C8−N3−N4−C9; Cg2: C10−C15; Cg3: C1−C6.
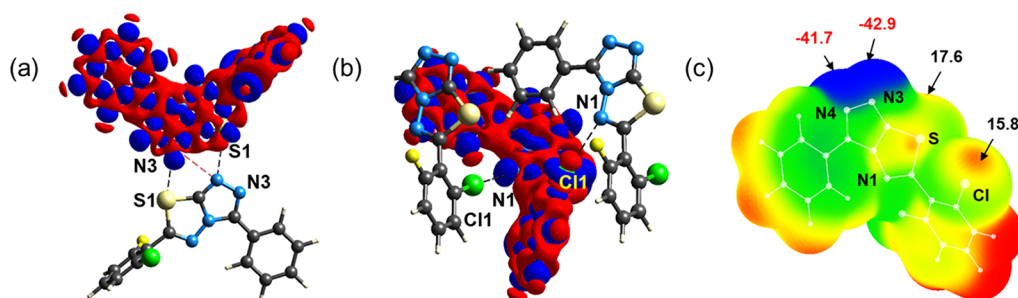

Figure 9. Deformation density maps for dimers (a) D2 and (b) D3 in **2** reveal the chalcogen and halogen bonds, respectively. (c) MESPs for structure **2** and the electron density surface drawn at 0.001 au contour. Color scales (in kcal mol⁻¹): red: >15; yellow: 15 to 0, green: 0 to −25; and blue: >−25. The small hemispheres indicate the selected positive ($V_{s,max}$; black) and negative ($V_{s,min}$; blue) electrostatic potentials along with their values.

in the inflammatory cell signaling pathway. The in vitro inhibitory activity of compounds **1** and **2** against these enzymes and the selectivity index (SI) are summarized in Table 4. The inhibition concentration (IC$_{50}$) values for control drugs, namely, celecoxib (selective COX-2 inhibitor) and diclofenac (non-selective COX inhibitor) are compared to assess the activity of compounds **1** and **2**. The in vitro data reveals that the binding affinity of compound **2** is nearly in 3-fold excess that of compound **1** toward the COX-1 enzyme. In contrast, the binding affinity of compound **1** is in 2-fold excess that of compound **2** toward the COX-2 enzyme. The assay results also indicate that molecule **1** with an adamantane moiety showed marked COX inhibitory activity with 10-fold

selectivity toward COX-2 (SI = 9.82) compared to molecule **2** with a phenyl ring in the place of adamantane cage. The result reveals the effect of the substituents (adamantane and phenyl) on the observed COX inhibition activity. Molecules containing 1,2,4-triazole have been reported to exhibit anti-inflammatory potential, and in our earlier reports we described the selective inhibitory potential of 4-(4-chlorophenyl)-3-[(4-fluorobenzyl)-sulfanyl]-5-(thiophen-2-yl)-4H-1,2,4-triazole with a COX-2 SI of 1.89.[35]

To corroborate in vitro data, we performed an in silico molecular docking analysis for the title compounds and two known drugs (diclofenac and celecoxib) with COX-1/2 enzymes. The GOLD docking program offered a better

Table 3. Topological Parameters for Selected Intermolecular Interactions in Different Dimers of Compounds 1 and 2[a]

interaction	R_{ij}	$\rho(r)$	$\nabla^2\rho(r)$	$V(r)$	$G(r)$	$H(r)$	$\|-V(r)/G(r)\|$	D_e
			compound **1**					
			D1					
H5A···N4	2.779	0.040	0.475	−7.8	10.4	2.6	0.75	0.9
F1A···N2	3.345	0.056	0.979	−15.6	21.1	5.5	0.74	1.9
			D4					
S1···C4A	3.340	0.071	0.774	−15.2	18.2	2.9	0.84	1.8
			D5					
H4A···N4	2.283	0.106	1.279	−23.9	29.4	5.4	0.81	2.9
			D6					
H12···Cl1A	3.050	0.031	0.393	−6.0	8.4	2.3	0.72	0.7
			compound **2**					
			D2					
S1···N3	2.808	0.132	1.525	−35.4	38.5	3.1	0.92	4.2
N3···N3	2.908	0.078	1.141	−22.5	26.8	4.3	0.84	2.7
			D3					
H11···Cl1	2.819	0.046	0.562	−9.2	12.3	3.0	0.75	1.1
Cl1···N1	3.231	0.050	0.696	−10.8	14.9	4.1	0.73	1.3
			D4					
H4···N4	2.548	0.069	0.825	−15.4	19.0	3.5	0.81	1.8
H5···N4	2.812	0.048	0.593	−10.4	13.3	2.9	0.78	1.2

[a]R_{ij}, bond path (Å); $\rho(r)$, electron density (e Å^{-3}); $\nabla^2\rho(r)$, Laplacian of electron density (e Å^{-5}); $V(r)$, potential electron density (kJ mol^{-1} br^{-3}); $G(r)$, kinetic electron density (kJ mol^{-1} br^{-3}); $H(r)$, total electronic energy density (kJ mol^{-1} br^{-3}); and D_e, dissociation energy (kcal mol^{-1}).

Table 4. In vitro COX-1 and COX-2 Inhibitory Activity and COX-2 Selectivity Index of Compounds 1 and 2, Celecoxib, and Diclofenac

	IC$_{50}$ (μM)[a]		SI[b]
	COX-1	COX-2	
compound **1**	26.12	2.66	9.82
compound **2**	8.50	5.44	1.56
celecoxib	21.60	0.07	308.57
diclofenac	2.72	3.02	0.90

[a]IC$_{50}$ value is the compound concentration required to produce 50% inhibition of COX-1 or COX-2 for means of three separate determinations. [b]SI (IC$_{50}$ COX-1/IC$_{50}$ COX-2).

performing ChemPLP fitness score for pose prediction,[64] which can be used to assess the binding potential of the compound, and a higher fitness score can be considered to be a better docking pose at the active site. Table 5 summarizes the

Table 5. ChemPLP Fitness Scoring Calculated Using the GOLD Molecular Docking Program

	COX-1		COX-2	
	ChemPLP score	MM-GBSA ΔG_{bind}	ChemPLP score	MM-GBSA ΔG_{bind}
compound **1**	66.0	−53.8	65.4	−58.4
compound **2**	60.3	−70.5	62.1	−59.8
celecoxib	80.0		65.4	
diclofenac	51.4		63.4	

ChemPLP fitness score for compounds **1** and **2** and two known COX inhibitors. The scores obtained agree well with the in vitro data. The relative affinity (ΔG_{bind}) of the COX-1/2-ligand (title compounds) was obtained using the MM-GBSA calculation. From ΔG_{bind} values, one can observe that compound **2** shows higher affinity toward COX-1 compared to COX-2, whereas both compounds display nearly equal

affinity toward the COX-2 enzyme (Table 5). Overall, the molecule with an adamantane moiety shows relatively higher binding potential with the active site of the COX-2 compared to COX-1, which is in good agreement with the in vitro data.

To understand the nature of noncovalent interaction formed between title compounds and COX enzymes, we analyzed the docked complexes (refined models using the MM-GBSA approach) using a PLIP Web server, as mentioned in the experimental section. Compound **1** establishes only hydrophobic interactions with the active site residues (Arg 120, Leu 352, Leu 359, Trp 387, Tyr 385, and Leu 531) of COX-1 (Figure 10a). It is noted that the di-substituted phenyl and adamantane moieties are involved in the hydrophobic interactions. As can be seen in Figure 10b, there is a relatively higher number of interactions (residues involved are as follows: Arg 120, Tyr 355, Leu 359, Phe 381, leu 384, Tyr 385, Trp 387, Leu 531, and Ala 527) established between compound **1** and the COX-2 enzyme compared to the corresponding COX-1 complex. This could a possible reason for the higher selectivity of compound **2** toward COX-2 enzymes.

Compound **2** showed relatively higher affinity compared to compound **1** for COX-1 according to the calculation of the MM-GBSA and the in vitro assay. It can be seen in Figure 10c, in addition to the higher number of hydrophobic interactions, the T-shaped π-stacking interaction between the di-substituted phenyl ring of **1** and a conserved Tyr 385 residue of COX-1 and a short F···O contact (backbone O atoms of the backbone of Met 522 and Ile 523 are involved). The unsubstituted phenyl ring also establishes hydrophobic interactions with the key residues. In the COX-2-compound **2** complex, both di-substituted and unsubstituted phenyl rings participate in hydrophobic interactions with the active site residues of COX-2 (Figure 10d). In addition, a hydrogen bond (O−H···N) formed between the central triazole ring and the Tyr 355 residue.
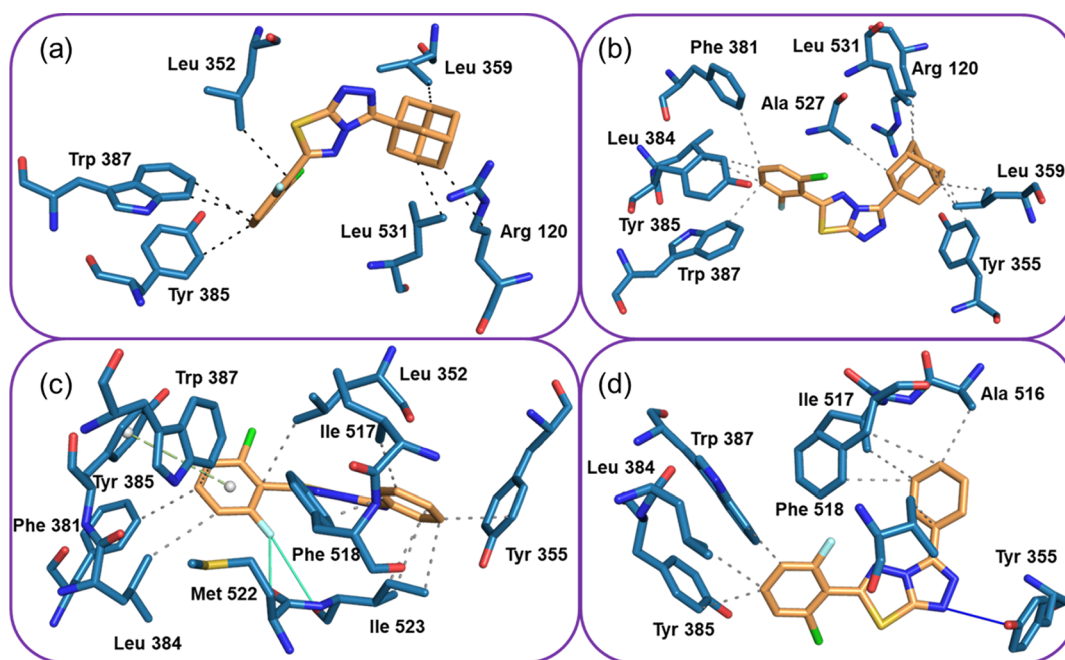
Figure 10. Active site residues of COX-1 and COX-2 establish noncovalent interactions with compounds **1** [(a) COX-1 and (b) COX-2] and **2** [(c) COX-1 and (d) COX-2].

3. CONCLUSIONS

The present study demonstrated the interplay of hydrogen, halogen, and chalcogen bonding in addition to π-stacking interactions in two compounds containing a [1,2,4]triazolo-[3,4-*b*][1,3,4]thiadiazole scaffold with adamantane and phenyl substituents. The X-ray structures and various theoretical tools were used to characterize the noncovalent interactions. Molecular conformation is locked by weak intramolecular C−H⋯N interactions in both compounds and one of the N atoms of the thiadiazole ring was involved as an acceptor. In related reported structures, the di-substituted ring was coplanar with the central triazolothiadiazole ring. The potential energy surface analysis revealed the preferred orientation of the di-substituted phenyl ring, which is in good agreement with the X-ray conformation of the investigated compounds. Through the crystal packing of compounds **1** and **2** are very similar (columnar packing mode), their basic structural motifs are different. The basic structural motif observed in **1** is stabilized by C−H⋯C(π), whereas the π-stacking interaction generates the basic structural motif in compound **2**. The solid-state structure of **1** was also stabilized by C−H⋯N, C−H⋯π, and C−H⋯Cl hydrogen bonds and a directional C−S⋯π chalcogen bond and unconventional short F⋯C/N contacts. Similarly, the solid-state structure of **2** was also stabilized by C−H⋯N, C−H⋯π, and C−H⋯Cl hydrogen bonds and directional attractive σ−hole interactions such as the C−Cl⋯N halogen bond and C−S⋯N chalcogen bond. In compound **2**, S(lp)⋯C(π) and a short N⋯N contacts play a supporting role in the stabilization of certain molecular dimers. The electrostatic potential surface map and the deformation density map revealed the characteristic features of σ−hole interactions. The contribution of H⋯H/Cl/N contacts was significantly varied due to the effect of phenyl/adamantane substituents, as evident from the HS analysis. The topological analysis suggested that the C−H⋯N interaction was found to be stronger in **1**, whereas C−S⋯N chalcogen bond was stronger in compound **2**. In vitro assay and in silico molecular coupling

and subsequent calculation of MM-GBSA free energy supported that the compound with an adamantane scaffold was 10-fold more selective against the COX-2 enzyme compared to compound **1**. This study identified that terminal groups (di-substituted and phenyl/adamantane moieties) are important in establishing noncovalent interactions with the active site residues of the COX-1/2 enzymes. In the future, these groups could be altered to improve the affinity and selectivity against these enzymes.

4. MATERIALS AND METHODS

4.1. Chemicals and Instruments. Melting points (°C, uncorrected) were measured in open glass capillaries using a Stuart SMP30 electro-thermal melting point apparatus. NMR spectra were obtained on a Bruker 400 Avance III at 400.20 MHz for ^{1}H and 100.63 MHz for ^{13}C using DMSO-d_6 as a solvent. Electrospray ionization mass spectroscopy (ESI-MS) was performed on an Agilent 6410 triple quad tandem mass spectrometer at 4.0 kV for positive ions. All chemical and solvents (HPLC grade) were purchased from commercial suppliers and were used without further purification. Monitoring the reactions and checking the purity of the final products were carried out by thin-layer chromatography using silica gel pre-coated aluminum sheets (60 F$_{254}$, Merck) and visualization was done with ultraviolet light (UV) at 365 and 254 nm.

4.2. Synthesis and Crystallization. A mixture of the corresponding 4-amino-5-substituted-4*H*-1,2,4-triazole-3-thiol (**C**)[41,42] (5.0 mmol), 2-chloro-6-fluorobenzoic acid (873 mg, 5.0 mmol), and phosphorous oxychloride (5 mL) was heated under reflux with stirring for 2 hours. On cooling, the reaction mixture was cautiously poured onto crushed ice (50 g) and the separated crude products were filtered, washed with saturated sodium hydrogen carbonate solution, and then with water, dried, and crystallized from EtOH/CHCl$_3$ to yield target compounds **1** and **2**.

4.2.1. 3-(Adamantan-1-yl)-6-(2-chloro-6-fluorophenyl)-[1,2,4]triazolo[3,4-b][1,3,4]thiadiazole 1. Colorless trapezoid crystals. Yield 1.64 g (84%); mp 288−290 °C. ^{1}H NMR (DMSO-d_6, 400.20 MHz): δ 1.78 (s, 6H, adamantane−H), 2.09 (s, 3H, adamantane−H), 2.17 (s, 6H, adamantane−H), 7.54 (d, 1H, Ar−H, J = 8.0 Hz), 7.64 (d, 1H, Ar−H, J = 8.0 Hz), 7.75−7.81 (m, 1H, Ar−H). ^{13}C NMR (DMSO-d_6, 100.64 MHz): δ 27.75, 34.76, 36.39, 39.25 (adamantane−C), 116.15, 123.50, 127.02, 134.32, 135.30, 159.54 (Ar−C), 154.09 (C5), 157.20 (C8), 162.10 (C2). Analysis for $C_{19}H_{18}ClFN_4S$ (388.89): C, 58.55 (calc. 58.68); H, 4.70 (calc. 4.67); N, 14.39 (calc. 14.41); S, 8.19 (calc. 8.24). ESI-MS m/z: 389.1 $(M + H, 100\%)^+$, 391 $(M + 2 + H, 37\%)^+$.

4.2.2. 6-(2-Chloro-6-fluorophenyl)-3-phenyl-[1,2,4]-triazolo[3,4-b][1,3,4]thiadiazole 2. Colorless plate crystals. Yield 1.19 g (72%); mp 253−255 °C. ^{1}H NMR (DMSO-d_6, 400.20 MHz): δ 7.56−7.67 (m, 5H, Ar−H), 7.77−7.83 (m, 1H, Ar−H), 8.24−8.26 (m, 2H, Ar−H). ^{13}C NMR (DMSO-d_6, 100.64 MHz): δ 115.91, 116.12, 125.69, 126.40, 126.98, 129.76, 131.03, 134.38, 135.48, 159.56 (Ar−C), 154.68 (C5), 158.92 (C8), 162.08 (C2). Analysis for $C_{22}H_{35}N_5O_2S$ (330.77): C, 54.41 (calc. 54.47); H, 2.51 (calc. 2.44); N, 16.78 (calc. 16.94); S, 9.95 (calc. 9.69). ESI-MS m/z: 331.0 $[M + H, 100\%]^+$, 333.0 $[M + 2 + H, 39\%]^+$.

4.3. Single-Crystal X-ray Diffraction. Single-crystal X-ray diffraction data were collected for crystals of compounds **1** and **2** at 160 (1) K on a Rigaku OD SuperNova/Atlas area-detector diffractometer using Cu Kα radiation (λ = 1.54184 Å) from a micro-focus X-ray source and an Oxford Instruments Cryojet XL cooler. The selected suitable single crystals were mounted using polybutene oil on a flexible loop fixed on a goniometer head and immediately transferred to the diffractometer. Pre-experiment, data collection, data reduction, and analytical absorption correction[65] were performed with the program suite CrysAlisPro, version 1.171.40.68a (Rigaku Oxford Diffraction, England, 2019). Using Olex2,[66] the structure was solved with the SHELXT[67] small-molecule structure solution program, and it was refined with the SHELXL2018/3 program package[68] by full-matrix least-squares minimization on F^2. In compound **1**, the substituted benzene was disordered over two sets of positions (labeled A and B) with site-occupancy factors of 0.7764(19) and 0.2236(19). All H atoms were placed in calculated positions (C−H = 0.95−0.99 Å) and were constrained to ride on their parent atoms, with $U_{iso}(H)$ = 1.2U_{eq}(C). The PLATON program was used to check the results of the X-ray analysis.[69] Crystal packing and molecular dimers were produced using the MERCURY program.[70]

4.4. Theoretical Calculations. For all calculations, we used the crystal structure geometry with the normalized H positions (C−H = 1.083 Å). Energy framework analysis[71,72] was performed on the CrystalExplorer-17.5 program[73] using the B3LYP/6-31G(d,p) level of approximation. The HS[74] and 2D-FP plots[75] were obtained from the CrystalExplorer-17.5 program. The deformation density was calculated for selected dimers at the HF/6-311G level using the CrystalExplorer program. We calculated the intermolecular interaction energies (E_{tot}) between molecular pairs using the CLP-PIXEL program.[76,77] For this computation, the electron density was obtained with the Gaussian 09 program[78] using MP2/6-31G** levels of theory. Furthermore, the accurate complexation energies of molecular pairs identified from the CLP-PIXEL energy calculation were calculated using the B97D3/def2-TZVP level of theory, and then, these complexation energies

were corrected (ΔE_{cp}) for the basis set superposition error using the counterpoise method.[79] The topological analysis of the selected dimers was performed within the framework of Bader's QTAIM approach using the AIMALL program.[80] The wave functions were calculated at the M062X-D3/def2-TZVP level of theory for topological analysis. The NCIplot index was also used to characterize the nature of noncovalent interactions.[81] The MESP surfaces have been constructed using the 0.001 a.u. isosurface with the program WFA-SAS.[82]

4.5. In Vitro COX Inhibition Assay. The in vitro inhibitory activity of compounds **1** and **2** against cyclo-oxygenases COX-1 and COX-2 was evaluated using an enzyme immunoassay kit of Cayman Chemical, Ann Arbor, MI, USA (catalog no. 560131). The preparation of the reagents and the testing procedure was performed according to the manufacturer recommendations using various concentrations (0.01− 100 μM) of compounds **1** and **2**, celecoxib (selective COX-2 inhibitor), and diclofenac (nonselective COX inhibitor) in dimethylsulfoxide (DMSO). The concentration that causes 50% enzyme inhibition (IC_{50}) was calculated from the concentration inhibition response curve and the SI was calculated by dividing IC_{50} COX-1 by IC_{50} COX-2.

4.6. Molecular Docking and Protein−Ligand Interaction Analysis. Docking studies were performed for compounds **1** and **2** and two control inhibitors, namely, celecoxib and diclofenac, using GOLD software.[64] Crystallographic structures of COX-1 (PDB ID: 3KK6; *Ovis aries* cyclooxygenase-1 complexed with celecoxib) and COX-2 (PDB ID: 5IKR; human cyclooxygenase-2 complexed with mefenamic acid) were obtained from Protein Data Bank (www.rcsb.org). Prior to docking simulations, the water molecules and cocrystallized ligands except celecoxib and mefenamic acid inhibitors were removed. All protein atoms within 6.0 Å of celecoxib and mefenamic acid inhibitors were used for the binding site definition.

The highest scoring poses (ChemPLP) of compounds **1** and **2** were also subjected to the MM-GBSA method to calculate the free energy (ΔG_{bind}) of the binding of ligands to target proteins using the Schrödinger suite (Schrodinger Release 2022-2, Schrödinger, LLC, New York, NY, 2021). In this calculation, the title compounds and active residues within 6 Å from the ligands were treated to be flexible and the remaining protein residues were kept frozen. Protein−ligand interactions for the docked complexes were analyzed using the PLIP Web server (protein−ligand interaction profiler).[83]

■ ASSOCIATED CONTENT

Ⓢ Supporting Information

The Supporting Information is available free of charge at https://pubs.acs.org/doi/10.1021/acsomega.2c04252.

> Topological properties for compounds **1** and **2**, molecular graphs for different dimers of **1** and **2**, and 2D-fingerprint plots for various intercontacts observed in **1** and **2** (PDF)

■ AUTHOR INFORMATION

Corresponding Authors

   Ali A. El-Emam − *Department of Medicinal Chemistry, Faculty of Pharmacy, Mansoura University, Mansoura 35516, Egypt;* ⊚ orcid.org/0000-0002-9325-9497; Email: elemam5@hotmail.com

Subbiah Thamotharan − *Biomolecular Crystallography Laboratory, Department of Bioinformatics, School of Chemical and Biotechnology, SASTRA Deemed University, Thanjavur 613 401, India;* ◉ orcid.org/0000-0003-2758-6649; Email: thamu@scbt.sastra.edu

Authors

Lamya H. Al-Wahaibi − *Department of Chemistry, College of Sciences, Princess Nourah bint Abdulrahman University, Riyadh 11671, Saudi Arabia*

Sekar Karthikeyan − *Biomolecular Crystallography Laboratory, Department of Bioinformatics, School of Chemical and Biotechnology, SASTRA Deemed University, Thanjavur 613 401, India*

Olivier Blacque − *Department of Chemistry, University of Zurich, Zurich 8057, Switzerland*

Amal A. El-Masry − *Department of Medicinal Chemistry, Faculty of Pharmacy, Mansoura University, Mansoura 35516, Egypt*

Hanan M. Hassan − *Department of Pharmacology and Biochemistry, Faculty of Pharmacy, Delta University for Science and Technology, Mansoura 11152, Egypt*

M. Judith Percino − *Unidad de Polímeros y Electrónica Orgánica, Instituto de Ciencias, Benemérita Universidad Autónoma de Puebla, San Pedro Zacachimalpa, Puebla-C.P. 72960, Mexico;* ◉ orcid.org/0000-0003-1610-7155

Complete contact information is available at:
https://pubs.acs.org/10.1021/acsomega.2c04252

Notes

The authors declare no competing financial interest.

■ REFERENCES

(1) Küçükgüzel, Ş. G.; Çıkla-Süzgün, P. Recent advances bioactive 1,2,4-triazole-3-thiones. *Eur. J. Med. Chem.* **2015**, *97*, 830−870.

(2) Aggarwal, R.; Sumran, G. An insight on medicinal attributes of 1,2,4-triazoles. *Eur. J. Med. Chem.* **2020**, *205*, 112652.

(3) Li, S. M.; Tsai, S. E.; Chiang, C. Y.; Chung, C. Y.; Chuang, T. J.; Tseng, C. C.; Jiang, W. P.; Huang, G. J.; Lin, C. Y.; Yang, Y. C.; Fuh, M. T.; Wong, F. F. New methyl 5-(halomethyl)-1-aryl-1*H*-1,2,4-triazole-3-carboxylates as selective COX-2 inhibitors and anti-inflammatory agents: Design, synthesis, biological evaluation, and docking study. *Bioorg. Chem.* **2020**, *104*, 104333.

(4) Ramalho, T. C.; Rocha, M.; da Cunha, E. F.; Freitas, M. P. The search for new COX-2 inhibitors: a review of 2002 - 2008 patents. *Expert Opin. Ther. Pat.* **2009**, *19*, 1193−1228.

(5) Jiang, B.; Zeng, Y.; Li, M. J.; Xu, J. Y.; Zhang, Y. N.; Wang, Q. J.; Sun, N. Y.; Lu, T.; Wu, X. M. Design, synthesis, and biological evaluation of 1,5-diaryl-1,2,4-triazole derivatives as selective cyclo-oxygenase-2 inhibitors. *Arch. Pharm. (Weinheim, Ger.)* **2010**, *343*, 500−508.

(6) Jiang, B.; Huang, X.; Yao, H.; Jiang, J.; Wu, X.; Jiang, S.; Wang, Q.; Lu, T.; Xu, J. Discovery of potential anti-inflammatory drugs: diaryl-1,2,4-triazoles bearing *N*-hydroxyurea moiety as dual inhibitors of cyclooxygenase-2 and 5-lipoxygenase. *Org. Biomol. Chem.* **2014**, *12*, 2114−2127.

(7) Navidpour, L.; Shafaroodi, H.; Abdi, K.; Amini, M.; Ghahremani, M. H.; Dehpour, A. R.; Shafiee, A. Design, synthesis, and biological

evaluation of substituted 3-alkylthio-4,5-diaryl-4*H*-1,2,4-triazoles as selective COX-2 inhibitors. *Bioorg. Med. Chem.* **2006**, *14*, 2507−2517.

(8) Abdellatif, K. R. A.; Abdelall, E. K. A.; Elshemy, H. A. H.; Philoppes, J. N.; Hassanein, E. H. M.; Kahk, N. M. Optimization of pyrazole-based compounds with 1,2,4-triazole-3-thiol moiety as selective COX-2 inhibitors cardioprotective drug candidates: Design, synthesis, cyclooxygenase inhibition, anti-inflammatory, ulcerogenic-ity, cardiovascular evaluation, and molecular modeling studies. *Bioorg. Chem.* **2021**, *114*, 105122.

(9) Cai, H.; Huang, X.; Xu, S.; Shen, H.; Zhang, P.; Huang, Y.; Jiang, J.; Sun, Y.; Jiang, B.; Wu, X.; Yao, H.; Xu, J. Discovery of novel hybrids of diaryl-1,2,4-triazoles and caffeic acid as dual inhibitors of cyclooxygenase-2 and 5-lipoxygenase for cancer therapy. *Eur. J. Med. Chem.* **2016**, *108*, 89−103.

(10) Tratrat, C. 1,2,4-Triazole: a privileged scaffold for the development of potent antifungal agents - a Brief Review. *Curr. Top. Med. Chem.* **2020**, *20*, 2235−2258.

(11) Peyton, L. R.; Gallagher, S.; Hashemzadeh, M. Triazole antifungals: a review. *Drugs Today* **2015**, *51*, 705−718.

(12) Strzelecka, M.; Świątek, P. 1,2,4-Triazoles as important antibacterial agents. *Pharmaceuticals* **2021**, *14*, 224.

(13) Li, J.; Zhang, J. The antibacterial activity of 1,2,3-triazole- and 1,2,4-triazole-containing hybrids against *Staphylococcus aureus*: An updated review (2020-present). *Curr. Top. Med. Chem.* **2022**, *22*, 41−63.

(14) Kaur, R.; Ranjan Dwivedi, A. R.; Kumar, B.; Kumar, V. Recent developments on 1,2,4-triazole nucleus in anticancer compounds: a review. *Anticancer Agents Med. Chem.* **2016**, *16*, 465−489.

(15) Wen, X.; Zhou, Y.; Zeng, J.; Liu, X. Recent development of 1,2,4-triazole-containing compounds as anticancer agents. *Curr. Top. Med. Chem.* **2020**, *20*, 1441−1460.

(16) Gay, C. M.; Balaji, K.; Byers, L. A. Giving AXL the axe: targeting AXL in human malignancy. *Br. J. Cancer* **2017**, *116*, 415−423.

(17) Hu, Y.; Li, C. Y.; Wang, X. M.; Yang, Y. H.; Zhu, H. L. 1,3,4-Thiadiazole: synthesis, reactions, and applications in medicinal, agricultural, and materials chemistry. *Chem. Rev.* **2014**, *114*, 5572−5610.

(18) Jain, A. K.; Sharma, S.; Vaidya, A.; Ravichandran, V.; Agrawal, R. K. 1,3,4-Thiadiazole and its derivatives: a review on recent progress in biological activities. *Chem. Biol. Drug Des.* **2013**, *81*, 557−576.

(19) Haider, S.; Alam, M. S.; Hamid, H. 1,3,4-Thiadiazoles: a potent multi targeted pharmacological scaffold. *Eur. J. Med. Chem.* **2015**, *92*, 156−177.

(20) Han, X.; Yu, Y. L.; Hu, Y. S.; Liu, X. H. 1,3,4-Thiadiazole: a privileged scaffold for drug design and development. *Curr. Top. Med. Chem.* **2021**, *21*, 2546−2573.

(21) Omar, Y. M.; Abdel-Moty, S. G.; Abdu-Allah, H. H. M. Further insight into the dual COX-2 and 15-LOX anti-inflammatory activity of 1,3,4-thiadiazole-thiazolidinone hybrids: The contribution of the substituents at 5th positions is size dependent. *Bioorg. Chem.* **2020**, *97*, 103657.

(22) Schenone, S.; Brullo, C.; Bruno, O.; Bondavalli, F.; Ranise, A.; Filippelli, W.; Rinaldi, B.; Capuano, A.; Falcone, G. New 1,3,4-thiadiazole derivatives endowed with analgesic and anti-inflammatory activities. *Bioorg. Med. Chem.* **2006**, *14*, 1698−1705.

(23) Kadi, A. A.; Al-Abdullah, E. S.; Shehata, I. A.; Habib, E. E.; Ibrahim, T. M.; El-Emam, A. A. Synthesis, antimicrobial and anti-inflammatory activities of novel 5-(1-adamantyl)-1,3,4-thiadiazole derivatives. *Eur. J. Med. Chem.* **2010**, *45*, 5006−5011.

(24) Janowska, S.; Paneth, A.; Wujec, M. Cytotoxic properties of 1,3,4-thiadiazole derivatives—a review. *Molecules* **2020**, *25*, 4309.

(25) Aliabadi, A. 1,3,4-Thiadiazole Based Anticancer Agents. *Anticancer Agents Med. Chem.* **2016**, *16*, 1301−1314.

(26) Wang, Y.; Li, L.; Zhang, B.; Xing, J.; Chen, S.; Wan, W.; Song, Y.; Jiang, H.; Jiang, H.; Luo, C.; Zheng, M. Discovery of novel disruptor of silencing telomeric 1-like (DOT1L) inhibitors using a target-specific scoring function for the (S)-adenosyl-l-methionine

(SAM)-dependent methyltransferase family. *J. Med. Chem.* **2017**, *60*, 2026–2036.

(27) Ningegowda, R.; Shivananju, N. S.; Rajendran, P.; Basappa; Rangappa, K. S.; Chinnathambi, A.; Li, F.; Achar, R. R.; Shanmugam, M. K.; Bist, P.; Alharbi, S. A.; Lim, L. H. K.; Sethi, G.; Priya, B. S. A novel 4,6-disubstituted-1,2,4-triazolo-1,3,4-thiadiazole derivative inhibits tumor cell invasion and potentiates the apoptotic effect of TNFα by abrogating NF-κB activation cascade. *Apoptosis* **2017**, *22*, 145–157.

(28) Zhang, L.; Zhao, J.; Zhang, B.; Lu, T.; Chen, Y. Discovery of [1,2,4]triazolo[3,4-*b*][1,3,4]thiadiazole derivatives as novel, potent and selective c-Met kinase inhibitors: Synthesis, SAR study, and biological activity. *Eur. J. Med. Chem.* **2018**, *150*, 809–816.

(29) Wu, J.; Li, J.; Xu, M. H.; Liu, D. Structure-activity relationship and interaction studies of new SIRT1 inhibitors with the scaffold of 3-(furan-2-yl)-[1,2,4]triazolo[3,4-*b*][1,3,4]thiadiazole. *Bioorg. Med. Chem. Lett.* **2014**, *24*, 3050–3056.

(30) Wu, S.; Shi, J.; Chen, J.; Hu, D.; Zang, L.; Song, B. Synthesis, Antibacterial activity, and mechanisms of novel 6-sulfonyl-1,2,4-triazolo[3,4-*b*][1,3,4]thiadiazole derivatives. *J. Agric. Food Chem.* **2021**, *69*, 4645–4654.

(31) Kamoutsis, C.; Fesatidou, M.; Petrou, A.; Geronikaki, A.; Poroikov, V.; Ivanov, M.; Soković, M.; Ćirić, A.; Carazo, A.; Mladěnka, P. Triazolo based-thiadiazole derivatives. Synthesis, biological evaluation and molecular docking studies. *Antibiotics* **2021**, *10*, 804.

(32) Chawla, G.; Kumar, U.; Bawa, S.; Kumar, J. Syntheses and evaluation of anti-inflammatory, analgesic and ulcerogenic activities of 1,3,4-oxadiazole and 1,2,4-triazolo[3,4-*b*]-1,3,4-thiadiazole derivatives. *J. Enzyme Inhib. Med. Chem.* **2012**, *27*, 658–665.

(33) Pathak, P.; Shukla, P. K.; Naumovich, V.; Grishina, M.; Verma, A.; Potemkin, V. 1,2,4-Triazole-conjugated 1,3,4-thiadiazole hybrid scaffolds: A potent ameliorant of carrageenan-induced inflammation by lessening proinflammatory mediators. *Arch. Pharm. (Weinheim, Ger.)* **2020**, *353*, 1900233.

(34) Tratrat, C.; Haroun, M.; Paparisva, A.; Kamoutsis, C.; Petrou, A.; Gavalas, A.; Eleftheriou, P.; Geronikaki, A.; Venugopala, K. N.; Kochkar, H.; Nair, A. B. New substituted 5-benzylideno-2-adamantylthiazol[3,2-*b*][1,2,4]triazol-6(5*H*)ones as possible anti-Inflammatory agents. *Molecules* **2021**, *26*, 659.

(35) Al-Wahaibi, L. H.; Rahul, B.; Mohamed, A. A. B.; Abdelbaky, M. S. M.; Garcia-Granda, S.; El-Emam, A. A.; Percino, M. J.; Thamotharan, S. Supramolecular self-assembly built by weak hydrogen, chalcogen, and unorthodox nonbonded motifs in 4-(4-chlorophenyl)-3-[(4-fluorobenzyl)sulfanyl]-5-(thiophen-2-yl)-4*H*-1,2,4-triazole, a selective COX-2 inhibitor: Insights from X-ray and theoretical studies. *ACS Omega* **2021**, *6*, 6996–7007.

(36) Al-Wahaibi, L. H.; Akilandeswari, G.; Anusha, R.; Al-Shaalan, N. H.; Alkmali, O. M.; El-Emam, A. A.; Percino, J. M.; Thamotharan, S. Insights into the nature of weak noncovalent interactions in 3-(4-fluorophenyl)-6-(2-fluorophenyl)-1,2,4-triazolo[3,4-*b*][1,3,4]-thiadiazole, a potential bioactive agent: X-ray, QTAIM and molecular docking analysis. *J. Mol. Struct.* **2019**, *1183*, 331–341.

(37) Khan, I.; Bakht, S. M.; Ibrar, A.; Abbas, S.; Hameed, S.; White, J. M.; Rana, U. A.; Zaib, S.; Shahid, M.; Iqbal, J. Exploration of a library of triazolothiadiazole and triazolothiadiazine compounds as a highly potent and selective family of cholinesterase and monoamine oxidase inhibitors: design, synthesis, X-ray diffraction analysis and molecular docking studies. *RSC Adv.* **2015**, *5*, 21249–21267.

(38) Khan, I.; Panini, P.; Khan, S. U.-D.; Rana, U. A.; Andleeb, H.; Chopra, D.; Hameed, S.; Simpson, J. Exploiting the role of molecular electrostatic potential, deformation density, topology, and energetics in the characterization of S···N and Cl···N supramolecular motifs in crystalline triazolothiadiazoles. *Cryst. Growth Des.* **2016**, *16*, 1371–1386.

(39) Novikov, A. S. Non-covalent interactions in organic, organometallic, and inorganic supramolecular systems relevant for medicine, materials science, and catalysis. *Crystals* **2022**, *12*, 246.

(40) Sharma, V.; Bhatia, P.; Alam, O.; Javed Naim, J. M.; Nawaz, F.; Ahmad Sheikh, A. A.; Jha, M. Recent advancement in the discovery and development of COX-2 inhibitors: Insight into biological activities and SAR studies (2008-2019). *Bioorg. Chem.* **2019**, *89*, 103007.

(41) Zhao, Y. Y.; Xing, Z.; Dai, W.; Han, G. F. 4-Amino-3-phenyl-1*H*-1,2,4-triazole-5(4*H*)-thione. *Acta Crystallogr., Sect. E: Struct. Rep. Online* **2008**, *64*, o1169.

(42) Al-Deeb, O. A.; Al-Omar, M. A.; El-Brollosy, N. R.; Habib, E. E.; Ibrahim, T. M.; El-Emam, A. A. Synthesis, antimicrobial, and anti-inflammatory activities of novel 2-[3-(1-adamantyl)-4-substituted-5-thioxo-1,2,4-triazolin-1-yl]acetic acids, 2-[3-(1-adamantyl)-4-substituted-5-thioxo-1,2,4-triazolin-1-yl]propionic acids and related derivatives. *Arzneim.-Forsch./Drug Res.* **2006**, *56*, 40–47.

(43) Groom, C. R.; Bruno, I. J.; Lightfoot, M. P.; Ward, S. C. The Cambridge Structural Database. *Acta Crystallogr., Sect. B: Struct. Sci.* **2016**, *72*, 171–179.

(44) Khan, M.-H.; Hameed, S.; Akhtar, T.; Stoeckli-Evans, H. 6-(Adamantan-1-yl)-3-(3-fluorophenyl)-1,2,4-triazolo[3,4-*b*][1,3,4]-thiadiazole. *Acta Crystallogr., Sect. E: Struct. Rep. Online* **2010**, *66*, o3215–o3216.

(45) Khan, M.-H.; Hameed, S.; Tahir, M. N.; Bokhari, T. H.; Khan, I. U. 6-(1-Adamantyl)-3-(2-fluorophenyl)-1,2,4-triazolo[3,4-*b*]-[1,3,4]thiadiazole. *Acta Crystallogr., Sect. E: Struct. Rep. Online* **2009**, *65*, o1437.

(46) Tahir, M. N.; Khan, M.-H.; Hammed, S.; Bokhari, T. H.; Hina, S. 6-(1-Adamantyl)-3-(2-chlorophenyl)-1,2,4-triazolo[3,4-*b*][1,3,4]-thiadiazole. *Acta Crystallogr., Sect. E: Struct. Rep. Online* **2011**, *67*, o1022.

(47) Khan, M.-H.; Akhtar, T.; Yasin, K. A.; Al-Masoudi, N. A.; Jones, P. G.; Hameed, S. Synthesis, crystal structure and antiproliferative activity of 6-adamantyl-3-aryl[1,2,4]triazolo[3,4-*b*][1,3,4]thiadiazoles. *Z. Naturforsch., A: Phys. Sci.* **2010**, *65*, 178–184.

(48) Al-Alshaikh, M. A.; Ghabbour, H. A.; Abdelbaky, M. S. M.; García-Granda, S.; El-Emam, A. A. Crystal structure of 6-(2-fluorophenyl)-3-phenyl-[1,2,4]-triazolo[3,4-*b*][1,3,4]thiadiazole, C$_{15}$H$_9$FN$_4$S. *Z. Krist.—NCS* **2016**, *231*, 661–663.

(49) Lei, X.-X.; Zhang, A.-J.; Huang, X.-B.; Zhang, L.-X. 6-(2-Chlorophenyl)-3-(4-ethoxyphenyl)-1,2,4-triazolo[3,4-*b*][1,3,4]-thiadiazole. *Acta Crystallogr., Sect. E: Struct. Rep. Online* **2006**, *62*, o4418–o4419.

(50) Swamy, S. N.; Basappa; Priya, B. S.; Prabhuswamy, B.; Doreswamy, B. H.; Prasad, J. S.; Rangappa, K. S. Synthesis of pharmaceutically important condensed heterocyclic 4,6-disubstituted-1,2,4-triazolo-1,3,4-thiadiazole derivatives as antimicrobials. *Eur. J. Med. Chem.* **2006**, *41*, 531–538.

(51) Nanjunda-Swamy, S.; Basappa; Sarala, G.; Prabhuswamy, B.; Anandalwar, S. M.; idhara-Prasad, J. S.; Rangappa, K. S. Synthesis and X-ray crystal studies of 6-(2-chlorophenyl)-3-methyl[1,2,4]triazolo-[4,5-*b*][1,3,4]thiadiazole. *J. Chem. Res.* **2005**, *2005*, 238–239.

(52) Al-Omary, F. A. M.; Ghabbour, H. A.; AlRabiah, H.; Al-Wahaibi, L. H.; El-Emam, A. A. Crystal structure of 6-(4-chlorophenyl)-3-(thiophen-2-yl)-[1,2,4]triazolo[3,4-*b*][1,3,4]-thiadiazole, C$_{13}$H$_7$ClN$_4$S$_2$. *Z. Krist.—NCS* **2016**, *231*, 931–932.

(53) Khan, I.; Ibrar, A.; Zaib, S.; Ahmad, S.; Furtmann, N.; Hameed, S.; Simpson, J.; Bajorath, J.; Iqbal, J. Active compounds from a diverse library of triazolothiadiazole and triazolothiadiazine scaffolds: synthesis, crystal structure determination, cytotoxicity, cholinesterase inhibitory activity, and binding mode analysis. *Bioorg. Med. Chem.* **2014**, *22*, 6163–6173.

(54) Holm, M.; Schollmeyer, D.; Laufer, S. 3-(2-Fluorophenyl)-6-(phenoxymethyl)-1,2,4-triazolo[3,4-*b*][1,3,4]thiadiazole. *Acta Crystallogr., Sect. E: Struct. Rep. Online* **2008**, *64*, o700.

(55) Du, H.-T.; Du, H.-J.; Zhou, W. 3,6-Bis(3,4,5-trimethoxyphenyl)-1,2,4-triazolo[3,4-*b*][1,3,4]thiadiazole. *Acta Crystallogr., Sect. E: Struct. Rep. Online* **2008**, *64*, o1577.

(56) Du, H.; Du, H.; An, Y.; Li, S. 6-(3-Pyridyl)-3-(3,4,5-trimethoxyphenyl)-1,2,4-triazolo[3,4-*b*][1,3,4]thiadiazole. *Acta Crystallogr., Sect. E: Struct. Rep. Online* **2008**, *64*, o1402.

(57) Du, H.; Du, H.; An, Y.; Li, S. 6-(2-Methylphenyl)-3-(3,4,5-trimethoxyphenyl)-1,2,4-triazolo[3,4-*b*][1,3,4]thiadiazole. *Acta Crystallogr., Sect. E: Struct. Rep. Online* **2008**, *64*, o1481.

(58) Du, H.-T.; Du, H.-J. 6-(4-Pyrid-yl)-3-(3,4,5-trimethoxy-phen-yl)-1,2,4-triazolo[3,4-*b*][1,3,4]thiadiazole. *Acta Crystallogr., Sect. E: Struct. Rep. Online* **2008**, *64*, o1634.

(59) Du, H. T.; Du, H. J.; Zhou, W. 6-(4-Methylphenyl)-3-(3,4,5-trimethoxy-phen-yl)-1,2,4-triazolo[3,4-*b*][1,3,4]thiadiazole. *Acta Crystallogr., Sect. E: Struct. Rep. Online* **2008**, *64*, o2040.

(60) Molina, P.; Arques, A.; Alias, M. A.; Saiz, A. L. L.; Concepción Foces-Foces, M. Ring-opening reactions of mesoionic [1,2,4]triazolo-[1,5-*c*]quinazolines.—preparation of 1,2,4-triazolo[3,4-*b*][1,3,4]-thiadiazoles by a translocative rearrangement. *Liebigs Ann. Chem.* **1989**, *1989*, 1055−1059.

(61) Dinçer, M.; Özdemir, N.; Çetin, A.; Cansız, A.; Büyükgüngör, O. 6-Phenyl-3-(4-pyridyl)-1,2,4-triazolo[3,4-*b*][1,3,4]thiadiazole. *Acta Crystallogr., Sect. C: Cryst. Struct. Commun.* **2005**, *61*, o665−o667.

(62) Naveen, S.; Swamy, S. N.; Basappa; Swamy, B. P.; Anandalwar, S. M.; Prasad, J. S.; Rangappa, K. S. Crystal structure of 3-*para* tolyl-6-(4′-methyl-biphenyl-2-yl)-[1,2,4]triazolo[3,4-*b*][1,3,4]thiadiazole. *Anal. Sci.: X-Ray Struct. Anal. Online* **2006**, *22*, x221−x222.

(63) Lu, D.; Zhang, M.; Song, L.; Tan, Q.; Shao, M. Ethyl 5-[6-(furan-2-yl)-1,2,4-triazolo[3,4-*b*][1,3,4]thia-diazol-3-yl]-2,6-dimethyl-nicotinate. *Acta Crystallogr., Sect. E: Struct. Rep. Online* **2008**, *64*, o80−o81.

(64) Jones, G.; Willett, P.; Glen, R. C.; Leach, A. R.; Taylor, R. Development and validation of a genetic algorithm for flexible docking. *J. Mol. Biol.* **1997**, *267*, 727−748.

(65) Clark, R. C.; Reid, J. S. The analytical calculation of absorption in multifaceted crystals. *Acta Crystallogr., Sect. A: Found. Crystallogr.* **1995**, *51*, 887−897.

(66) Dolomanov, O. V.; Bourhis, L. J.; Gildea, R. J.; Howard, J. A. K.; Puschmann, H. A. OLEX2: A complete structure solution, refinement and analysis program. *J. Appl. Crystallogr.* **2009**, *42*, 339−341.

(67) Sheldrick, G. M. SHELXT—integrated space-group and crystal-structure determination. *Acta Crystallogr., Sect. A: Found. Adv.* **2015**, *71*, 3−8.

(68) Sheldrick, G. M. Crystal structure refinement with SHELXL. *Acta Crystallogr., Sect. C: Struct. Chem.* **2015**, *71*, 3−8.

(69) Spek, A. L. Structure validation in chemical crystallography. *Acta Crystallogr., Sect. D: Biol. Crystallogr.* **2009**, *65*, 148−155.

(70) Macrae, C. F.; Bruno, I. J.; Chisholm, J. A.; Edgington, P. R.; McCabe, P.; Pidcock, E.; Rodriguez-Monge, L.; Taylor, R.; van de Streek, J.; Wood, P. A. Mercury CSD 2.0—new features for the visualization and investigation of crystal structures. *J. Appl. Crystallogr.* **2008**, *41*, 466−470.

(71) Turner, M. J.; Thomas, S. P.; Shi, M. W.; Jayatilaka, D.; Spackman, M. A. Energy frameworks: insights into interaction anisotropy and the mechanical properties of molecular crystals. *Chem. Commun.* **2015**, *51*, 3735−3738.

(72) Mackenzie, C. F.; Spackman, P. R.; Jayatilaka, D.; Spackman, M. A. CrystalExplorer model energies and energy frameworks: extension to metal coordination compounds, organic salts, solvates and open-shell systems. *IUCrJ* **2017**, *4*, 575−587.

(73) Turner, M. J.; McKinnon, J. J.; Wolff, S. K.; Grimwood, D. J. *CrystalExplorer17*; University of Western Australia, 2017.

(74) Spackman, M. A.; Jayatilaka, D. Hirshfeld surface analysis. *CrystEngComm* **2009**, *11*, 19−32.

(75) Spackman, M. A.; McKinnon, J. J. Fingerprinting intermolecular interactions in molecular crystals. *CrystEngComm* **2002**, *4*, 378−392.

(76) Gavezzotti, A. Calculation of intermolecular interaction energies by direct numerical integration over electron densities. I. Electrostatic and polarization energies in molecular crystals. *J. Phys. Chem. B* **2002**, *106*, 4145−4154.

(77) Gavezzotti, A. Calculation of intermolecular interaction energies by direct numerical integration over electron densities. 2. An improved polarization model and the evaluation of dispersion and repulsion energies. *J. Phys. Chem. B* **2003**, *107*, 2344−2353.

(78) Frisch, M. J.; Trucks, G. W.; Schlegel, H. B.; Scuseria, G. E.; Robb, M. A.; Cheeseman, J. R.; Scalmani, G.; Barone, V.; Mennucci, B.; Petersson, G. A.; Nakatsuji, H.; Caricato, M.; Li, X.; Hratchian, H. P.; Izmaylov, A. F.; Bloino, J.; Zheng, G.; Sonnenberg, J. L.; Hada, M.; Ehara, M.; Toyota, K.; Fukuda, R.; Hasegawa, J.; Ishida, M.; Nakajima, T.; Honda, Y.; Kitao, O.; Nakai, H.; Vreven, T.; Montgomery, J. A., Jr.; Peralta, J. E.; Ogliaro, F.; Bearpark, M. J.; Heyd, J.; Brothers, E. N.; Kudin, K. N.; Staroverov, V. N.; Kobayashi, R.; Normand, J.; Raghavachari, K.; Rendell, A. P.; Burant, J. C.; Iyengar, S. S.; Tomasi, J.; Cossi, M.; Rega, N.; Millam, N. J.; Klene, M.; Knox, J. E.; Cross, J. B.; Bakken, V.; Adamo, C.; Jaramillo, J.; Gomperts, R.; Stratmann, R. E.; Yazyev, O.; Austin, A. J.; Cammi, R.; Pomelli, C.; Ochterski, J. W.; Martin, R. L.; Morokuma, K.; Zakrzewski, V. G.; Voth, G. A.; Salvador, P.; Dannenberg, J. J.; Dapprich, S.; Daniels, A. D.; Farkas, Ö.; Foresman, J. B.; Ortiz, J. V.; Cioslowski, J.; Fox, D. J. *Gaussian 09*, Revision D.01; Gaussian, Inc.: Wallingford, CT, USA, 2013.

(79) Boys, S. F.; Bernardi, F. The calculation of small molecular interactions by the differences of separate total energies. Some procedures with reduced errors. *Mol. Phys.* **1970**, *19*, 553−566.

(80) Keith, T. A. *AIMAll*, version 19.02.13; TK Gristmill Software: Overland Park, KS, 2019.

(81) Contreras-García, J.; Johnson, E. R.; Keinan, S.; Chaudret, R.; Piquemal, J.-P.; Beratan, D. N.; Yang, W. NCIPLOT. A program for plotting non-covalent interaction regions. *J. Chem. Theory Comput.* **2011**, *7*, 625−632.

(82) Bulat, F. A.; Toro-Labbé, A.; Brinck, T.; Murray, J. S.; Politzer, P. Quantitative analysis of molecular surfaces: areas, volumes, electrostatic potentials and average local ionization energies. *J. Mol. Model.* **2010**, *16*, 1679−1691.

(83) Adasme, M. F.; Linnemann, K. L.; Bolz, S. N.; Kaiser, F.; Salentin, S.; Haupt, V. J.; Schroeder, M. PLIP 2021: expanding the scope of the protein-ligand interaction profiler to DNA and RNA. *Nucleic Acids Res.* **2021**, *49*, W530−W534.